Bachelor's Thesis

Studien zur CP-Quantenzahl des Higgs-Bosons

Studies on the CP-quantum numbers of the Higgs boson

prepared by

Paul Konstantin Krug

from Göttingen

at the II. Institute of Physics Göttingen

Abstract

Studies on the CP quantum numbers of the Higgs boson were performed. The impact parameter method, the ρ-decay plane method and the combination of both methods, all described in [1], were implemented in C++ and applied to Monte-Carlo generated samples for different CP mixing angles of a $125\,\text{GeV}$ Higgs boson at the LHC ($\sqrt{s} = 13\,\text{TeV}$) on truth-level. The relevant Higgs decay channel is $h \to \tau\tau$. The impact of various different parameters on the CP sensitive φ^*_{CP} distribution has been studied. Detector uncertainties were simulated by applying Gaussian smearing to the key quantities. The precision on the CP-mixing angle has been estimated, taking into account gluon-gluon-fusion, vector-boson-fusion as well as the DRELL-YAN-background from $Z \to \tau\tau$. It was found that the achievable precision is $\Delta\phi_\tau = 21°$ at a luminosity of $120\,\text{fb}^{-1}$. However, it was also found that the precision could be improved to $\Delta\phi_\tau = 17°$ by an enhanced application of the CP analysing methods.

Keywords: CP quantum number of the Higgs boson, CP mixing angle

Zusammenfassung

Studien zur CP-Quantenzahl des Higgs-Bosons wurden durchgeführt. Die Stoßparameter-Methode, die ρ-Zerfallsebenen-Methode und die Kombination beider Methoden, welche allesamt in [1] beschrieben werden, wurden in C++ implementiert und mit Hilfe von Monte-Carlo-generierten Ereignissen getestet. Dabei wurden verschiedene CP-Quantenzahlen für ein $125\,\text{GeV}$ Higgs-Boson bei einer Schwerpunktsenergie von $\sqrt{s} = 13\,\text{TeV}$ simuliert. Der untersuchte Zerfallskanal des Higgs-Teilchens war $h \to \tau\tau$. Die Auswirkungen verschiedener Parameter auf die CP-sensitive φ^*_{CP}-Winkelverteilung wurden untersucht. Experimentelle Messungenauigkeiten wurden mit Hilfe von Gauß-verteilten Zufallszahlen für die wichtigsten Größen simuliert. Die Präzision, mit der ein CP-Mischungswinkel ϕ_τ bestimmt werden kann, wurde für eine Luminosität von $120\,\text{fb}^{-1}$ ermittelt. Die dafür untersuchten Prozesse waren die Gluon-Gluon-Fusion, die Vektor-Boson-Fusion und der DRELL-YAN-Untergrund $Z \to \tau\tau$. Die ermittelte Unsicherheit für den Mischungswinkel beträgt $\Delta\phi_\tau = 21°$. Allerdings konnte die Präzision durch eine verbesserte Anwendung der entsprechenden Methoden auf $\Delta\phi_\tau = 17°$ erhöht werden.

Stichwörter: CP-Quantenzahl des Higgs-Bosons, CP-Mischungswinkel

Contents

1. Introduction

Around 450 B.C., the Greek philosopher EMPEDOCLES established his Classical-element-theory, which describes the whole universe as a composition of the four elements -fire, air, water and earth. Today, almost 2500 years later, we are very certain about those assumptions to be false. Nowadays the corresponding aspect of philosophy has been replaced by the science of particle physics, although its aspiration remains the same: The understanding of the universe by its fundamental constituents and laws, expressed in a *theory of everything* (ToE). While the works of EMPEDOCLES and other antique philosophers mark the origin of attempts to describe nature by its elementary structures, only the beginning of the 19th century saw growing evidence for the real existence of atoms, which were believed to be the smallest, indivisible particles. However, the end of the 19th century culminated in the discovery of the electron by EMIL WIECHERT and JOSEPH JOHN THOMSON as well as the first observation of radioactivity by ANTOINE HENRI BECQUEREL, leading to the recognition of subatomic structures. The following development of quantum mechanics during the early 20th century gave rise to a lot of different atomic theories, all suffering either from theoretical problems or from lacking ability to describe newer observations. Therefore a satisfying description of atoms and molecules was not available until the theory of atomic orbitals was finally set up in the 1920s. Nevertheless, dealing with the smallest reachable structures has to be particle physics' nature by definition. Consequently a deeper understanding of nature was gained by the research on nuclear physics within the following years. The 1950s saw the door to modern particle physics finally be pushed open, as a result of powerful particle accelerators becoming available on the one hand, as well as the development of new quantum field theories (QFT) on the other hand. One did not only observe unknown particles and nuclear substructures but also discovered new forces beside electromagnetism and gravitation, which are called the weak and the strong interaction. The fundamental particles and forces then got structured within unified theories such as the electroweak theory in 1968, based on achievements of SHELDON GLASHOW [2], STEVEN WEINBERG [3] and ABDUL SALAM [4]. After the strong force was also included during the 1970s [5], the electroweak theory eventually progressed into a powerful unified field theory, that we call the *Standard Model*

1. Introduction

of particle physics (SM).

A topic of prime interest in modern particle physics regards to the observation of a large matter/antimatter-asymmetry in the universe: while theory predicts particle-creation in matter/antimatter-pairs, we do not observe the universe[1] to be a matter/antimatter-mixture but almost an exclusive formation of ordinary matter. Mathematically this asymmetry reflects as a violation of the *charge conjugation parity symmetry* (CP), which is a combination of charge conjugation symmetry (inversion of charge sign) and parity symmetry (inversion of spatial coordinates). Although the Standard Model introduces CP violation via the weak interaction, this mechanism is not sufficient to explain the observed asymmetries' magnitude. In fact, that is why different beyond Standard Model CP violating mechanisms are expected to exist by many.

In July 2012, the ATLAS- and CMS-Collaborations at the European Organization for Nuclear Research (CERN) announced the Higgs boson to be discovered [6, 7]. The existence of a Higgs boson was one of the most important predictions for about half a century and therefore a strong test of the Standard Model. However, to ascertain if the observed Higgs particle is indeed the Standard Model boson, one has to measure its properties and check them against the SM predictions. The characteristics in question, not only include the particles' spin and couplings, but also the corresponding CP-quantum number, which is prognosticated to be CP-even (CP=+1) by the Standard Model. Whereas the pure CP-odd case (CP=-1) can already be excluded by experiment, the found Higgs boson could still turn out to be a composition of CP-even and -odd components, as it is well known that quantum mechanics allows for mixed states. If this were indeed the case, a new form of CP violation could be observed in the Higgs-sector. This fact alone spells out the importance of studies on the Higgs bosons' CP-nature. Appropriate studies were performed within this thesis. They are performed using Monte-Carlo-generated data on truth-level[2]. Therefore, they can obviously not reach the significance of real data analysis, but state the corresponding facts as well as pave the way to reconstruction-level/real data studies by demonstrating and validating the substantial methods in Higgs-CP analysis.

---

[1]The reference here is the baryonic part of the universe. As pointed out later on, the universe consists only to 5 % of baryonic matter. Baryons are particles, composed of three quarks, for example protons and neutrons.

[2]Truth-level means that all kind of parameters and quantities are potentially accessible. No interaction with a detector is simulated.

2. The Standard Model of particle physics

The verbalization "Standard Model of particle physics" describes a theory, which unifies three forces of nature, namely, the electromagnetic, the weak and the strong force. Moreover, it characterises all known particles in the field of subatomic physics that take part in those interactions. In particular, the model describes elementary particles, which can be divided into *fermions* and *bosons*, see Chapter (2.1). In terms of mathematics, the Standard Model turns out to be a gauge quantum field theory, which respects the internal symmetries of the unitary product group $SU(3)_C \otimes SU(2)_I \otimes U(1)_Y$. While the group $SU(3)_C$ classifies the strong interaction, the gauge theory of the electroweak interaction is described by $SU(2)_I \otimes U(1)_Y$ [4]. Since Noether's theorem states that every continuous symmetry of action implies a corresponding conservation law, a conserved charge (such as the weak hypercharge Y, the weak Isospin I or the colour charge C) can be assigned to each particle participating in a relevant interaction.

The Standard Model has to be mathematically self-consistent and renormalizable. Besides, its formulation is chosen to satisfy special relativity.

Almost all theoretical quantities predicted by the Standard Model have been experimentally studied and the corresponding results agree with the theory. Most importantly, all elementary particles, which were only predicted by the theory, eventually were observed, such as the top-quark (1995) [8, 9], the tau-neutrino (2000) [10] or, most recently, the Higgs boson (2012) [6, 7]. So far, no experimental events were observed worldwide that would conflict with the Standard Model explicitly up to a 5-σ confidence level[1].

---

[1]In terms of statistical significance, more than $99.9999\,\%$ of a normal distribution is expected to lie within an interval of five standard derivations (5-σ). The chance that an observed signal just dues to a statistical fluctuation, is therefore extremely low. In particle physics a 5-σ confidence level is a common requirement in order to announce a discovery.

2.1. Elementary particles of the Standard Model

Fermions

The Standard Model contains twelve fundamental fermions (particles with half-integer spin) and of course, their corresponding antiparticles. All elementary fermions are spin-$1/2$ particles. The fermions can be divided into six *leptons* and six *quarks*, which are further separated into three generations, see Figure (2.1). Each generation is composed of a pair of leptons and a pair of quarks, so that every generation carries a total of four fundamental particles. Namely, they consist of an up-type quark ($Q = +2/3$), a down-type quark ($Q = -1/3$) a charged lepton ($Q = -1$) and the respective lepton-neutrino ($Q = 0$) [2–4]. While the three generations differ among themselves primarily in their particles' mass (for example the top quark is about 75000 times heavier than the up quark), the constituents within a single generation also vary in their behaviour with respect to the different interactions. In detail, the quarks interact via the electromagnetic, the weak and strong force, whereas the leptons only respond to the electromagnetic and the weak interaction. However, due to their lack of an electric charge, lepton-neutrinos only interact weakly[2]. As a reason of name convention, the elementary fermions and all further particles consisting of elementary fermions are used to be called "matter". In contrary, compositions of the fermions' antiparticles are labelled as "antimatter".
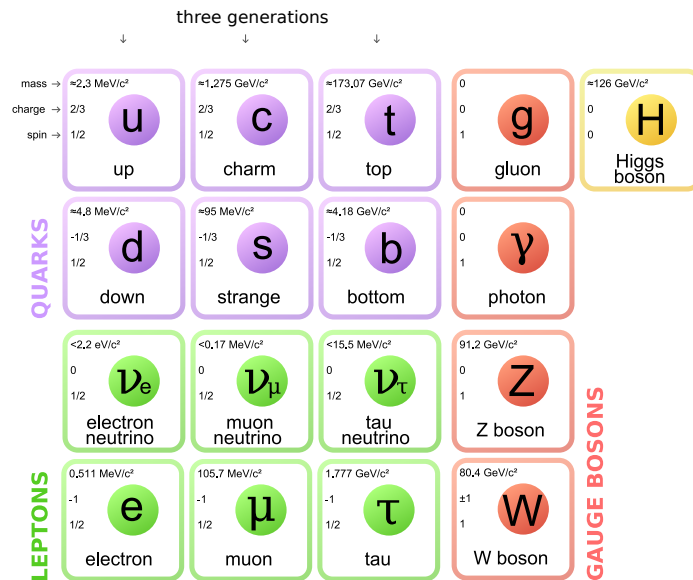

Figure 2.1.: The elementary particles and gauge bosons of the Standard Model.

[2] All massive particles also underlie the force of gravitation. However this interaction is negligibly small unless it happens at energies near the PLANCK scale $\sim 10^{19}$ GeV, which is far from achievable with modern technology.

Vector bosons

In the Standard Model describes physical interactions through the exchange of bosons (particles with an integer spin value, whereas spin-1 particles are called vector bosons). Thereby, the theory knows four vector bosons. Those are called gauge bosons and should be considered as the field quanta of the corresponding interactions. Mathematically it is termed an adjoint representation[3] of the underlying symmetry group. The mediator of the electromagnetic interaction is the photon. It is the gauge boson of the $U(1)_Y$ group. Furthermore, it is a massless particle and does not hold any electric charge ($Q = 0$). Those properties both result in the infinite range of the electromagnetic interaction and also lead to the macroscopic observability of photons.

Within the Standard Model, the strong force is described by the $SU(3)_C$. Since the corresponding representations for the $SU(N)$ groups of the Standard Model are $N^2 - 1$-dimensional, there exist eight types of gluons. They directly incorporate the generators of the subjacent gauge group and differ among each other in their colour wave functions. Gluons carry two (non vanishing) colour charges and therefore, they participate in their own interaction. As a result, gluon self-coupling will happen and the corresponding self-coupling terms have to be introduced to the Standard Model Lagrangian. Consequently, the strong coupling constant α_s acts very different compared to the electroweak coupling: the running constant α_s grows at low energies and large distances. Hence, isolating colour charged particles from each other turns out to be impossible. New particle/antiparticle-pairs will be created if the energy, stored in the colour field, exceeds a certain threshold energy needed to produce those particles. This phenomenon, known as "confinement", explains why one is not able to observe free carriers of colour charges, with exception of the top quark: the top quark lifetime ($\approx 5 \cdot 10^{-25}\,\mathrm{s}$) is even shorter than the time scale of hadronisation. Therefore, the top quark is the only colour charged particle that allows for studies of its "bare" properties. Due to confinement, the strong force gets effectively limited to a range of about $10^{-15}\,\mathrm{m}$, even though the gluons are massless particles.

The force carriers of the weak interactions are called $W^\pm$ and Z^0 bosons. The W bosons carry an electric charge ($Q = \pm 1$) and the Z boson is uncharged. In contrast to the photon and gluons, the gauge bosons of the weak force turn out to be massive particles. While the W boson weighs approximately $80\,\mathrm{GeV}$, the Z boson is even heavier with a mass of roughly $91\,\mathrm{GeV}$. Due to exchange particles of this high mass, the weak forces' range of influence gets restricted to the order of $10^{-18}\,\mathrm{m}$.

In the first instance, massive gauge bosons and fermions constitute a major problem for

---

[3]Through an adjoint representation, the elements of a Lie group are described as linear transformations of the corresponding Lie algebra [11].

the Standard Model, because the gauge fields must not contain any mass terms as long as one calls for local gauge invariance[4]. Only the spontaneous breaking of the gauge symmetry, with the help of an additional field, leads to a working mechanism for particles to gain mass.

2.2. Electroweak symmetry breaking and the Higgs mechanism

The spontaneous breaking of the electroweak symmetry is necessary in order to provide mass terms to the SM Lagrangian without violating local gauge invariance. The symmetry is broken through the BROUT-ENGLERT-HIGGS-mechanism [12, 13], which introduces the Higgs field. This field is ever-present in space and fills out the vacuum. However, the mechanism also requires the existence of an excitation of the Higgs field, which we call Higgs boson.

Symmetry breaking of a scalar field & BEH-mechanism

One considers a complex-valued scalar field ϕ composed of the real fields ϕ_1 and ϕ_2:

$$\phi = \frac{1}{\sqrt{2}}\left(\phi_1 + i\,\phi_2\right), \tag{2.1}$$

with the Lagrangian [14]:

$$\mathcal{L} = \underbrace{\left(\partial_\mu\,\phi\right)^\dagger\left(\partial^\mu\,\phi\right)}_{\text{Kinetic term}} - \underbrace{\mu^2\left(\phi^\dagger\,\phi\right)}_{\text{Mass term}} - \underbrace{\lambda\left(\phi^\dagger\,\phi\right)^2}_{\text{Interaction term}}, \tag{2.2}$$

where $\mu^2\left(\phi^\dagger\,\phi\right) + \lambda\left(\phi^\dagger\,\phi\right)^2$ is the potential term with a global $U(1)$ symmetry. That means the potential remains invariant under the transformation $\phi \to \phi' = e^{i\,Q}\,\phi$, since $\phi'^\dagger\,\phi' = \phi^\dagger\,\phi$. In order to describe a physical vacuum state, the potential is required to have a minimum and therefore $\lambda > 0$. For $\mu^2 > 0$, the potential takes the shape of a two dimensional parabola with a single minimum at $\phi_1 = \phi_2 = 0$. However, for $\mu^2 < 0$ one gets an infinite amount of minima (a two dimensional ring, see Figure (2.2)) at:

$$\phi_1^2 + \phi_2^2 = -\frac{\mu^2}{\lambda} \equiv \nu^2, \tag{2.3}$$

---

[4]Local gauge invariance is an important concept in theoretical particle physics. The dynamics of particles is required to be invariant under local transformations of certain parameters.

where ν is the "vacuum expectation value". The physical vacuum state will occur at the minima and it will break the global $U(1)$ symmetry of $\mathcal{L}$. As a comparison, one can consider a ball, which is spontaneously rolling down a hill and therefore breaks the rotational symmetry. Without loss of generality, it is possible to choose the vacuum state to be in the real direction $(\phi_1, \phi_2) = (\nu, 0)$. This way, one simplifies the math for the following operations, but the physics remains the same[5].

One now rewrites the scalar fields expanded at the vacuum state in order to describe physical particles and interactions:

$$\phi_1(x) = \eta(x) + \nu, \tag{2.4}$$

$$\phi_2(x) = \xi(x), \tag{2.5}$$

$$\phi = \frac{1}{\sqrt{2}}\left(\eta + \nu + i\,\xi\right), \tag{2.6}$$

where $\eta(x) = \xi(x) = 0$ at the minimum. The corresponding Lagrangian can then be rewritten as:

$$\mathcal{L} = \underbrace{-\frac{1}{4}\lambda\,\nu^4}_{\text{Constant term}} + \underbrace{\lambda\,\nu^2\,\eta^2}_{\text{Mass term}} + \underbrace{\lambda\,\nu\,\eta^3 + \frac{\lambda}{4}\,\eta^4 + \frac{\lambda}{4}\,\xi^4 + \lambda\,\nu\,\eta\,\xi^2 + \frac{1}{2}\,\lambda\,\eta^2\,\xi^2}_{\text{Physical interation terms}}, \tag{2.7}$$

$$\equiv \frac{1}{2}\left(\partial_\mu\,\eta\right)\left(\partial^\mu\,\eta\right) - \frac{1}{2}\,m_\eta^2\,\eta^2 + \frac{1}{2}\left(\partial_\mu\,\xi\right)\left(\partial^\mu\,\xi\right) - V_{\text{int}}(\eta, \xi), \tag{2.8}$$

where the mass terms are $m_\eta = \sqrt{2\,\lambda\,\nu^2}$ and $m_\xi = 0$. The term $V_{\text{int}}(\eta, \xi)$ describes the physical interaction of the massive scalar field η and the massless scalar field ξ, whose excitations are NAMBU-GOLDSTONE bosons. According to Goldstone's theorem, a breaking of a continuous symmetry implies the existence of those massless scalar particles.

Electroweak symmetry breaking in the Standard Model

Within the Standard Model, the BEH-mechanism has to be applied to a $SU(2)_L \otimes U(1)_Y$ group product. Therefore, one needs three degrees of freedom (d.o.f) from Goldstone bosons to provide the longitudinal d.o.f for the $W^\pm$ and Z^0 masses and one d.o.f for the Higgs mass. Longitudinal d.o.f lead to massive particles. Massless particles cannot have longitudinal d.o.f, otherwise parts of the field would travel faster than light.

However, to achieve the d.o.f, one considers two complex scalar fields, a neutral one and a

---

[5]If the vacuum state was in an arbitrary direction, the chosen basis would be different from the mass-eigenstate basis. The emerging terms would be harder to interpret physically. However, one could then rotate the potential and rewrite the Lagrangian in terms of the transformed potential to obtain the same results.
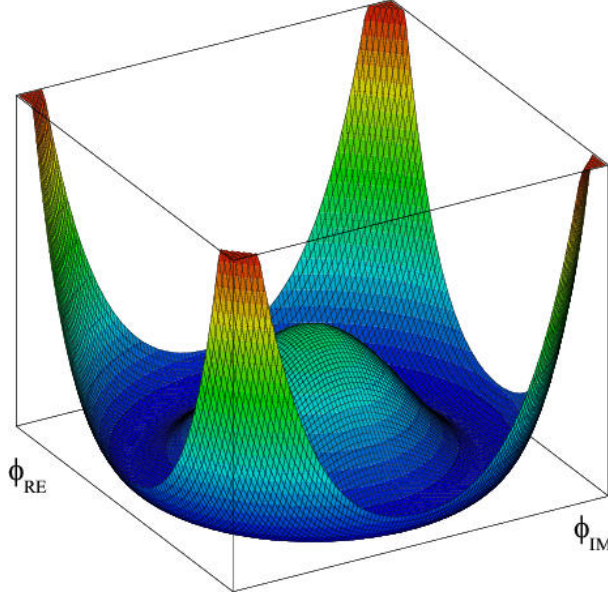
Figure 2.2.: The form of the Higgs potential.

charged one (for the charged bosons). The fields are then placed into an isospin doublet:

$$\phi = \begin{pmatrix} \phi^{\pm} \\ \phi^{0} \end{pmatrix} = \frac{1}{\sqrt{2}} \begin{pmatrix} \phi_1 + i\,\phi_2 \\ \phi_3 + i\,\phi_4 \end{pmatrix} \tag{2.9}$$

Then, as reported in the previous section, the Lagrangian can be re-written in terms of the electroweak gauge fields and finally ends up with one massive scalar field (Higgs boson) and three d.o.f for the longitudinal polarisations of the gauge bosons. Three bosons obtain a mass ($W^{\pm}$, Z^0), and one gauge boson remains massless (γ). The fermion masses are also introduced by coupling to the Higgs field, whereby a stronger coupling means a larger mass. Finally, the Higgs boson also couples to itself. The described couplings to bosons and fermions are visualised in the following Lagrangian [14]:

$$\mathcal{L} = \underbrace{-g_{Hf\bar{f}}\,f\bar{f}H}_{\text{Higgs to fermion coupling}} + \underbrace{\frac{g_{HHH}}{6}\,H^3 + \frac{g_{HHHH}}{24}\,H^4}_{\text{Higgs self-coupling}} + \underbrace{\delta_V\,V_\mu V^\mu \left(g_{HVV}\,H + \frac{g_{HHVV}}{2}\,H^2 \right)}_{\text{Higgs to gauge boson coupling}}, \tag{2.10}$$

where $V = W^{\pm}$ or Z^0 and $\delta_W = 1$, $\delta_Z = 1/2$. The coupling constants are the following:

$$g_{Hf\bar{f}} = \frac{m_f}{\nu}, \quad g_{HVV} = \frac{2\,m_V^2}{\nu}, \quad g_{HHVV} = \frac{2\,m_f^2}{\nu^2} \tag{2.11}$$

$$g_{HHH} = \frac{3\,m_H^2}{\nu}, \quad g_{HHHH} = \frac{3\,m_H^2}{\nu^2}. \tag{2.12}$$

The Higgs boson

The Higgs boson is an elementary particle of the Standard Model with no electric charge ($Q = 0$), spin-0 and even parity ($J^P = 0^+$). The particle was named after the British physicist PETER HIGGS, who won the Nobel Prize for the theoretical development of the Higgs mechanism together with FRANÇOIS ENGLERT in 2013.

For a long time, the discovery of the Higgs boson was the most important goal of the scientists at CERN, as well as one of the strongest tests on the Standard Model. The Higgs mechanism is a necessary part of the Model and the Higgs boson, as an excitation of the Higgs field, was predicted by the theory.

In July 2012, the discovery of a spin-0 resonance with a mass of 125 GeV was announced by the European Organisation for Nuclear Research (CERN) [6, 7]. The particle is consistent with the Standard Model Higgs. However, a precise investigation in the particles' properties is still ongoing.

At the LHC, the main Higgs production modes are gluon-gluon-fusion (ggH) and vector boson fusion (VBF), see Figure (2.3). The most important decay modes are $H \to \gamma\gamma$, $H \to ZZ \to \ell^+\ell^-\ell^+\ell^-$, $H \to W^+W^- \to \ell^+\nu\ell^-\bar{\nu}$, $H \to \tau^+\tau^-$ and $H \to b\bar{b}$.
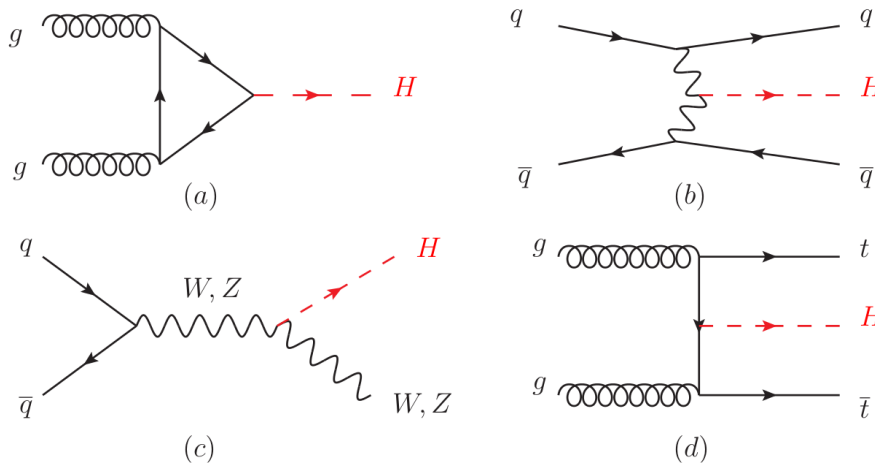

Figure 2.3.: Feynman diagrams of the four major Higgs production processes. At the LHC, the gluon-gluon-fusion (a) and vector-boson-fusion (b) are the most important production channels. The channel (c) is called Higgs-strahlung and (d) is associated production with top quarks [14].

2.3. Limits of the Standard Model

Despite the fact that the Standard Model always provided correct predictions and does not conflict with any experimental results, most particle physicists do not feel very satisfied by this theory. The reason lies in the numerous scientific-sensitive questions left open by the Standard Model.

Gravitation

The actual formulation of the Standard Model does not include the fourth force of nature, the gravitation. Solely on that ground, the theory has to be incomplete. Further, the most up to date theory of gravity is given by general relativity (GR), which seems to be mathematically incompatible with the framework of quantum field theory. Since gravity turns out to be not renormalizable, non-vanishing divergencies occur in higher order calculations of gravitational processes. Thus, useful predictions of process amplitudes are not possible.

While the usual scope of application usually require only one of the two theories (GR for large-scales and high-mass regions such as stars, galaxies, etc., and on the other hand QFT for small-scale and low-mass regions, such as molecules, atoms, etc.), the lack of a quantum gravity becomes a major challenge in areas of extreme mass/energy or low scales, such as under the conditions existing within a black hole or during early stages after the Big Bang.

Dark matter and dark energy

From the measurements of galaxies' rotational velocities by observing Doppler shifts, it is known that baryonic matter constitutes only 5% of the universes' total energy. Roughly 26% is made of so called "dark matter" [15], which does seem to interact with the Standard Model fields. Mainly via gravitational effects, the dark matter becomes noticeable. However, its nature is problematic with regards to theory, since the Standard Model does not predict any particles that would make up reasonable candidates for dark matter. Certainly, some supersymmetric expansions of the Standard Model take pleasure to popularity, because they are introducing possible dark matter candidates. Thereby, supersymmetry is a hypothetical symmetry that relates between bosons and fermions.

Nevertheless, about 69% of the universe is filled out by a "dark energy" [15]. Thereby it is about a constant energy density, which fills out the vacuum and leads to an increasing cosmic inflation. Attempts made via the Standard Model in order to explain the dark

energy as a vacuum energy, lead to a mismatch in 56 orders of magnitude: since the Higgs potential fills out the whole space, it should contribute to the vacuum energy (i.e. to the cosmological constant Λ from the EINSTEIN equation). However, the calculated value is 10^{56} times larger than the measured value for the dark energy density and also has the opposite sign [16].

Neutrino masses

The Higgs mechanism is not giving mass to neutrinos, therefore the Standard Model describes neutrinos to be massless. Nonetheless, neutrino-oscillation-experiments [17, 18] resulted in evidence for neutrinos to have mass. Neutrino oscillation is a process in quantum mechanics, that allows neutrinos, which were created with a certain flavour, to change its flavour over time. The probability to measure a certain flavour oscillates periodically as the neutrino travels through space. The mechanism, allowing neutrinos to gain mass is not explicitly clear and no real element of the Standard Model.

CP violation

As already mentioned in the introduction, one would expect about equal amounts of matter and antimatter during the beginning of the universe. However, large regions in space, dominated by antimatter should be observable via gamma ray detection. Since those are not seen, we observe a large matter/antimatter asymmetry, which is not to be explained by the Standard Models' CP violating mechanisms. Further, one of those mechanisms eventually leads to another concern, known as the "strong CP problem".

Strong CP problem

Theoretically, the QCD-Lagrangian should feature natural terms, allowing for a CP violation [19, 20]:

$$\mathcal{L} = -\frac{1}{4} F_a^{\mu\nu} F_{\mu\nu}^a - \frac{\theta\, g^2}{32\, \pi^2} F_a^{\mu\nu} \tilde{F}_{\mu\nu}^a + \bar{\psi} \left(i\, \gamma^\mu\, D_\mu - m\, \exp\left(i\, \alpha\, \gamma^5 \right) \right) \psi. \tag{2.13}$$

The second term violates both parity and time reversal invariance [20]. Since it conserves charge conjugation, it must violate CP[6]. The complex exponential in the mass term arises, if one also considers chiral transformations. Consequently CP symmetry should be violated within quantum chromodynamics for non-vanishing values of the arbitrary

---

[6]In quantum field theory, the CPT-theorem is a fundamental law. It states that every physical process is invariant under a simultaneous transformation of charge parity, parity and time reversal.

angle θ and the chiral phase α. However, the strong interaction is not observed to violate CP. This means that the terms in question are at least very close to zero, leading to a problem of *fine-tuning*. One has to keep in mind that fine-tuning of physical constants is not making a wrong theory, but is often referred to be calling out for an underlying mechanism, able to explain why a certain value has to be fine-tuned. The next problem is also related to this context.

Number of parameters

The Standard Model shows at least 19 free parameters (nine masses for the quarks and leptons, three mixing angles and one complex phase for the CKM-matrix, three gauge couplings, one QCD vacuum angle, the vacuum expectation value of the Higgs potential and the mass of the Higgs boson) [21], which remain unpredicted. Since those have to be determined by experiment, some charge the Standard Model with getting a certain adaptability to experimental results and wish for a subjacent theory, not only explaining the origin of the parameters, but ideally also predicting them.

Hierarchy problems

Inter alia, hierarchy problems refer to the big differences in the coupling strength of the natural forces. In particular it is about the question why the weak force is about 32 orders of magnitude stronger than gravitation.

More generally speaking, hierarchy problems typically occur in the renormalization process of masses or coupling constants. Again, fine-tuning problems are likely to arise (for example in the Higgs mass), if delicate cancellations of loop-corrections take place: in quantum mechanical calculations of amplitudes, one also has to consider contributions from higher order processes. If certain loop-corrections have the same magnitude but opposite sign, they can cancel out each other. In case of the Higgs mass, one measures a relatively light mass. However, considering higher order contributions, the mass is expected to be very large unless cancellation happens.

Among numerous expansions of the Standard Model, many other models exist, such as with extra dimensions, string theory, loop quantum gravity, etc., which are able to solve some of the introduced problems but mostly at the expense of involving new unanswered questions. Additionally, many of these theories can not be experimentally verified at the moment. As a consequence there is no theory up to now, acceptably sophisticated and mathematically consistent that could replace the Standard Model.

3. The experimental setup

3.1. The Large Hadron Collider

The Large Hadron Collider (LHC) is both the most complex and biggest single machine on earth as well as the worlds' most powerful particle accelerator with regards to the center-of-mass (COM) energy. The collider is located at CERN near Geneva. The LHC was built from 1998 until 2008. Over 10,000 scientists and engineers from over 100 different countries around the world work in collaborations on different experiments at the LHC.

The colliders' main task is to scrutinise the theoretical predictions of (high-energy) physics, as well as helping to investigate unsolved physical problems. In the end, it should contribute to a deeper understanding of the physical phenomena that we observe in our universe. In particular, studies on the Higgs boson belong to the most important duties of the LHC.

While the collider was designed with a center-of-mass energy of $\sqrt{s} = 14\,\text{TeV}$ in mind, it was initially running at an energy of $7\,\text{TeV}$, during the years from 2010 until 2012. That means each beam carried an energy of about $3.5\,\text{TeV}$, since the LHC is a symmetric collider. For colliders in general, the COM energy is given by $\sqrt{s} = \sqrt{4\,E_1\,E_2}$ with the energies E_1 and E_2 of the respective beams. In 2012 the COM energy was increased to $\sqrt{s} = 8\,\text{TeV}$. Afterwards, in February of 2013, the collider was shut down. The following two years saw a phase of upgrading, which enabled the LHC to run at the premeditated energy of $14\,\text{Tev}$. From April 2015, the COM energy in proton-proton collisions reached $13\,\text{Tev}$.

The structure of the Large Hadron Collider

The LHC's main-colliding-ring is a synchrotron accelerator, featuring a $26.7\,\text{km}$ beam pipe within a toroidal tunnel, more than $50\,\text{m}$ beneath the earth's surface. The collider operates as a proton and lead nuclei accelerator. Those particles are accelerated to velocities close to the speed of light and are then brought to collision. Via a complex arrangement of pre-accelerators, the particles can be coupled into the main accelerator, or alternatively

be decoupled from it.

The LHC features several detectors, that record the signatures of particles during the corresponding collisions. Those detectors may cover different purposes depending on their experimental requirements and therefore widely differ in size, mass and structure. Namely, the detectors and their corresponding experiments are called ATLAS, CMS, LHCb, ALICE, LHCf, TOTEM and MOEDAL.

Luminosity

When it comes to particle colliders, an important quantity is given by the *instantaneous luminosity*. This variable describes the number of collisions, which happen within a certain time and area. In order to make discoveries, one needs to get a sufficient amount of data, or scientifically spoken, a sufficient integrated luminosity. Having a higher instantaneous luminosity, means that the relevant data can be collected within a shorter period of time. While the general expression for the luminosity is

$$L = \frac{1}{\sigma} \frac{d\,N}{dt},$$
(3.1)

with σ labelling the event cross-section and dN means the number of events detected within a certain time interval dt, it can be calculated in the case of a colliding ring via:

$$L = \frac{n \cdot N_1 \cdot N_2 \cdot f}{A}.$$
(3.2)

Thereby the variables N_1 and N_2 quantify the number of particles per bunch[1] in the corresponding beams. While the number of bunches is given by n, their cross sectional area is described by the parameter A. Last but not least the colliding frequency is then given by f.

With a peak-luminosity of $9.0 \cdot 10^{33}\,\mathrm{cm^{-2}\,s^{-1}}$, the LHC is holding the luminosity world record for proton accelerators (situation June 2016). However, the future is anticipated to see the LHC reaching luminosities in the order of $10^{34}\,\mathrm{cm^{-2}\,s^{-1}}$.

Current research at the LHC

The first run at the LHC lasted from 2009 until 2013. No evidence for new particles were found during the first year. From the data collected in 2010, one could primarily set limits on theoretical models.

---

[1]A particle beam is not to be visualised as a continuous stream but rather as small particle bunches following each other.

In 2011 it was reported, that quark-gluon plasma states, which are believed to be the most dense manifestations of matter beyond black holes, were produced. While the data from 2011 could be used to estimate upper and lower bounds on the Higgs mass, the discovery of a new particle with a mass of 125 GeV succeeded in July 2012, combining the data from 7 and 8 TeV COM energy. In all probability, this one reveals as the long searched Higgs boson. Furthermore, some new hadrons were observed in the data of the LHCs' first run. Results published in July 2015 were consistent with the existence of penta-quark states (bound states consisting of five quarks) in the lambda-baryon decay.

During the second run, the LHC operates at a higher center-of-mass energy than ever before. First results on supersymmetric physics and exotic models were published by ATLAS and CMS in December 2015, for example [22]. Interestingly, both collaborations saw a slight excess in the invariant-mass spectra of two-photon-events at roughly 750 GeV [23]. With the data collected until the end of 2016 one should be able to decide if this turns out to be a real signal or a statistical fluctuation.

Future plans

First of all, the luminosity of the LHC will be raised constantly until 2018, in order to collect as much data as possible at $\sqrt{s} = 13$ TeV center-of-mass energy. Thereby, an increase in energy to 14 TeV would be feasible. During 2018 a conversion phase should be initiated. The corresponding upgrade aims to further increase the luminosity up to an order of $10^{35}\,\mathrm{cm^{-2}\,s^{-1}}$. Besides, several detectors, such as ALICE and CMS will probably be upgraded for the purpose of a better resolution. The inner parts of ATLAS will also be upgraded.

Nonetheless, another upgrade could double the COM energy in distant future, if novel technology would allow for boosting the field strength of the used magnets significantly (from 8.3 Tesla now to around 20 Tesla [24]).

The LHCs' term is expected to end by 2030.

3.2. The ATLAS detector

ATLAS is a toroidal particle detector at the LHC, with a diameter of 25 m and a length of about 46 m. The detector weighs roughly 7,000 tons. More than 7,600 scientist from over 215 countries worldwide participate in the ATLAS experiment. In terms of physical research, ATLAS is a "multi-purpose" detector. It is both about testing different theoretical predictions, as well as the search for new physics beyond the Standard Model.

The structure of the ATLAS detector

The detector features a shell structure, which is typical for collision experiments. The inner part is composed of a four-layer *silicon-pixel detector*, that provides a high resolution regarding the particle-interaction vertices. Thereby, the innermost part near the beam pipe is covered by the *Insertable B-Layer* (IBL), which was only introduced in the second run of the LHC. The IBL was inserted in order to recover from possible failures of the pixel detector. However, it also provides a powerful contribution to the determination of vertices, particle tracking and b-tagging[2]. A *silicon-strip detector* encloses the inner part. This element allows to determine the trajectories of particles passing through it. The inner detector is completed by a *transition radiation tracker* (TRT), which can be used to distinguish electrons from hadrons. The arrangement is surrounded by a solenoid magnet with a field strength of 2 Tesla. If a charged particle enters the magnetic field, its trajectory gets bent. The particles' momentum can then be measured from the corresponding curvature.

The *electromagnetic calorimeter* is located directly adjacent to the magnet. It is composed of lead-absorbers, layered with liquid argon, which can be used as an active detector material, because it gets ionised by electromagnetically interacting particles. By applying an electric field, the ions begin to drift. Thereby they induce a charge, allowing for a measurement of the corresponding particle energy.
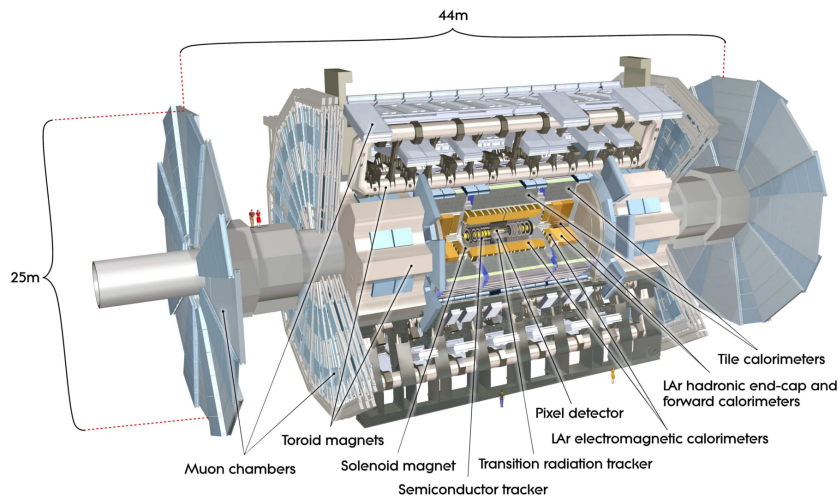

Figure 3.1.: The structure of the ATLAS detector.

In order to determine the energy of hadrons, the *hadronic calorimeter* is used. Consist-

---

[2]The term "b-tagging" describes a method, used in experimental particle physics, in order to identify particle-jets which originate from b quarks.

ing of steel-plates layered with synthetic scintillators, it allows to read out the light pulses that occur in the scintillators as a consequence of the particle showers taking place in the steel plate if a high-energy particle penetrates the calorimeter. Near the beam axis, layers of copper and wolfram are inserted to improve the calorimeters' radiation hardness.

Muons deposit their energy in the *muon chambers*. Since muons are minimal ionising particles, they hardly lose energy in the calorimeters. In order to measure the muon momenta, the muon chambers are interfused with a strong magnetic field of 4 Tesla, provided by a toroidal magnet.

When the LHC is running at full capacity, ATLAS is generating an enormous amount of data: roughly 25 megabyte of raw data are produced per event. Since around 40 million beam crossings happen within a second, the total amount of raw data lies in the order of petabyte per second. However, this turns out to be far more than one could process or store with modern technology. Therefore, a sophisticated system of event-triggers is reducing the quantity of data to a volume of about 100 events per second, respectively around 100 megabytes per second. A visualisation of the ATLAS trigger system is given by Figure (3.2).
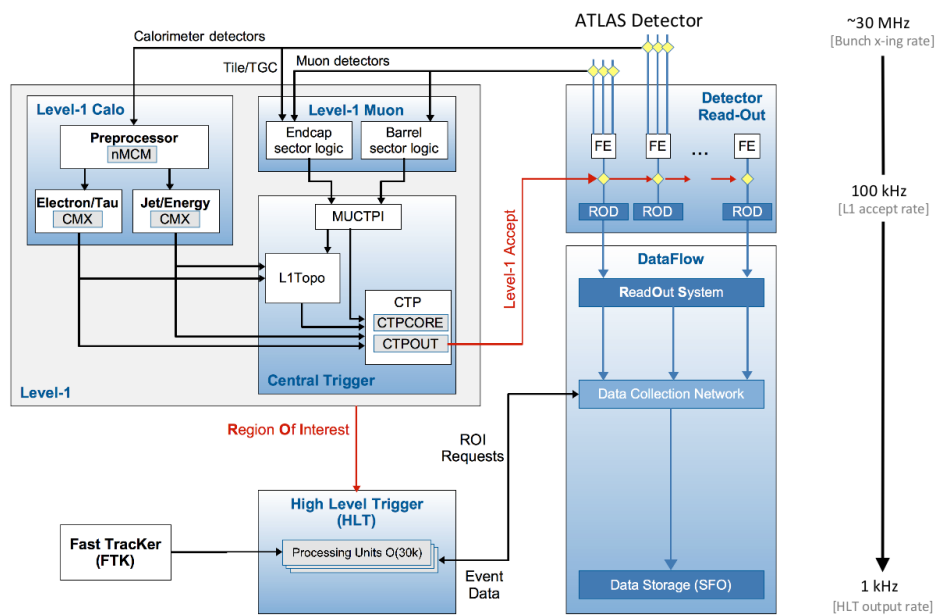

Figure 3.2.: Schematic layout of the Run-2 ATLAS trigger system.

4. Methods of the Higgs CP-analysis

4.1. Introduction to the Higgs CP-analysis

The analyses (based on a luminosity of $5\,\mathrm{fb}^{-1}$ at $\sqrt{s} = 7\,\mathrm{TeV}$ and $20\,\mathrm{fb}^{-1}$ at $\sqrt{s} = 8\,\mathrm{TeV}$) on both the mass as well as on the production and decay rates of the $h(125\,\mathrm{GeV})$ Higgs boson, published by the ATLAS and CMS collaborations, mark the end of a successful first run at the LHC [25].

Actually, the investigation in the Higgs bosons' properties, in particular its quantum numbers is a subject of recent research and of prime interest, since one has to make sure whether the observed resonance is really the Standard Model Higgs boson or not. In detail, four essential properties need to be studied: the spin quantum number (SM prediction: 0), the CP quantum number (+1), the coupling to fermions and vector bosons (proportional to their mass), Higgs self-coupling (proportional to its mass).

The investigations in the production and decay rates of the $h(125\,\mathrm{GeV})$ resonance reveal its properties to be consistent with the Standard Model Higgs boson. In particular, the spin-0 nature of the particle has been demonstrated. Spin-1 models ($J^P = 1^+, 1^-$) or exotic models with a graviton-like spin ($J^P = 2^+$) could be excluded by results extracted from the $H \to VV^*$ ($V = Z^0, W^\pm$) and $H \to \gamma\gamma$ decay channels [26].

Measurements of the couplings to fermions and massive bosons show the expected linear behaviour [27], while the effective research on the Higgs self-coupling probably has to wait for a higher luminosity [28]. However, studies on the Higgs CP sector are already possible with the available data. In particular, the possibility of a pure, pseudoscalar Higgs boson ($J^P = 0^-$) was disfavoured by analyses on angular correlations from H decays into VV^* final states. This certainly does not mean that the $h(125\,\mathrm{GeV})$ resonance is a pure scalar state ($J^P = 0^+$), because a CP-odd particle would not show a tree level[1] coupling to VV^* states. Only induced by quantum fluctuations, a coupling to the CP-odd component would then be very small. Therefore, a corresponding process could mainly project out the scalar component of the HVV^* coupling. In concrete terms that means that the

---

[1]A tree level coupling means a process at lowest order (no contributions from loops and higher order processes).

bosonic decay channels do not provide any insight in a possible CP-mixed state [26]. The question, if the found Higgs boson is CP-mixed or not, remains and turns out to be very relevant, since a mixing would conflict with the Standard Model and constitute evidence for new physics.

A promising approach of investigating in the Higgs bosons' CP-nature is given by a measurement of spin correlations in the $h \to \tau^+\tau^-$ decay channel. This channel does not only have a relatively high branching ratio ($6\,\%$), but fermions also couple to a pseudoscalar component at tree level [29]. The general Yukawa interaction between h and τ-leptons can be expressed via [30]:

$$\mathcal{L}_Y = -\frac{m_\tau}{\nu}\, k_\tau \,\left(\cos\left(\phi_\tau\right) \bar{\tau}\,\tau + \sin(\phi_\tau)\, \bar{\tau}\, i\, \gamma^5\, \tau\right)\, h. \tag{4.1}$$

The parameter $\nu = 246\,\text{GeV}$ denotes the vacuum expectation value of the Higgs field and $k_\tau > 0$ describes the reduced Yukawa coupling strength. The CP violation is parametrised via the CP mixing angle ϕ_τ. For $\phi_\tau = 0$ the Higgs particle h will only couple to scalar fermion currents. Vice versa, with an angle of $\phi_\tau = \pm\frac{\pi}{2}$, h will only couple to pseudoscalar fermion currents. If it couples to both currents, one will observe a CP mixture and the angle will necessarily take on a non-trivial value. In order to get access to this mixing angle, the spin-correlations in the τ decays have to be studied. As one can read of from the differential decay width, the corresponding information is encoded in the relation of transversal spin components[2] [1]:

$$d\Gamma_{h\to\tau^+\tau^-} \sim 1 - s_z^-\, s_z^+ + \cos(2\,\phi_\tau)\left(s_T^- \cdot s_T^+\right) + \sin(2\,\phi_\tau)\left(\left(s_T^+ \times s_T^-\right)\cdot \hat{k}^-\right), \tag{4.2}$$

where $\hat{k}$ denotes the normalised momentum of the τ lepton, $s_z^\pm$ describes the longitudinal and $s_T^\pm$ the transversal component of the unit spin vector $\hat{s}^\pm$ (in the corresponding $\tau^\pm$ rest frame), with respect to $\hat{k}^-$. Both combinations $\hat{s}^-$, $\hat{k}^-$ and $\hat{s}^+$, $\hat{k}^-$ define a certain plane. By measuring the angular distributions between these $\tau^\pm$-decay planes, one can draw conclusions on the CP quantum number of the Higgs boson. However, since the experimental situation at the LHC does not allow for a reconstruction of the $\tau^+\tau^-$ zero-momentum-frame (ZMF) or the $\tau^\pm$ rest frame, it is a main task to find useful observables which are sensitive to a CP-mixed state without a reconstruction of those frames.

One method, the so called *impact parameter method*, can be applied to all decay channels, where the $\tau^\pm$ decays into one or three charged prongs ($a^\pm$). The final charged particles from the $\tau^+\tau^-$ decays are denoted by a^- and a'^+. Another method, the *ρ-decay plane method*, is only applicable to the $\tau^+\tau^- \to \rho^+\rho^- + 2\,\nu_\tau$ decay mode but turns out to be more

---

[2]This relation holds for $\beta_\tau = \sqrt{1 - 4\,m_\tau^2/m_h^2} \approx 1$.

precise than the impact parameter method in this channel. Nevertheless, the combination of both methods leads to a higher precision in the $\tau^\pm \tau^\mp \to \rho^\pm a^\mp + X$ channels [1]. The normalised angular distributions for the decay of polarised $\tau^\pm$ leptons to charged prongs $a^\pm$ are described (in the τ rest frame) by the following equation [30, 31]:

$$\Gamma_a^{-1} d\Gamma_a \left(\tau^\pm(\hat{s}^\pm) \to a^\pm(q^\pm) + X \right) = n(E_{a^\pm}) \left(1 \pm b(E_{a^\pm}) \, \hat{s}^\pm \cdot \hat{q}^\pm \right) dE_{a^\pm} \frac{d\Omega_{a^\pm}}{4\pi}, \qquad (4.3)$$

where $E_{a^\pm}$ and $\hat{q}^\pm$ are the energies and unit momenta of the $a^\pm$ particles in their corresponding τ rest frame. While the decay rate $\tau \to a$ is described by the function $n(E_{a^\pm})$, the τ-spin analysing power of $a^\pm$ is encoded in $b(E_{a^\pm})$. Those functions are called spectral functions and they are given in [31]. Although they are not an explicit subject of this analyses, they still play a very important role, since $b(E_{a^\pm})$ has a major influence on the shape of the angular distribution.

In this analysis, all important one and three prong tau decay modes have been studied:

$$\tau \to \pi + \nu_\tau, \qquad (4.4)$$

$$\tau \to \rho + \nu_\tau \to \pi + \pi^0 + \nu_\tau, \qquad (4.5)$$

$$\tau \to a_1^{L,T} + \nu_\tau \to 2\,\pi^\pm + \pi^\mp + \nu_\tau, \qquad (4.6)$$

$$\tau \to a_1 + \nu_\tau \to \pi + 2\,\pi^0 + \nu_\tau, \qquad (4.7)$$

$$\tau \to \ell + \nu_\tau, + \nu_l, \qquad (4.8)$$

where (L, T) denote the longitudinal and transversal polarisations of the a_1 resonance. Both states can be separated by their kinematics. However, this was not done in this analyses, since the corresponding distributions were not available. The lepton in Equation (4.8) can be an electron or muon.

One should keep in mind that the τ-spin analysing power is maximal for the direct decays $\tau^\pm \to \pi^\pm$ and $\tau\pm \to a_1^{L,T\,\pm}$. The spin analysing powers of the other decays are rather small, but they can be improved by applying certain kinematic cuts [30, 31].

4.2. The impact parameter method

The impact parameter method (IP method) is described in [1, 29–31]. The method is decay mode independent and therefore it can be used for the Channels (4.4) - (4.8). It only requires a non-zero impact parameter of the charged prongs $a^\pm$ and $a'^\mp$. The impact parameter describes the smallest distance between two particles that would occur if they would not feel any force field. In this case, the impact parameter vectors begins

at the Higgs production vertex, which is almost equal to its production vertex due to the extreme short lifetime of the Higgs ($\approx 10^{-22}$ s). The impact parameter vectors end on the extrapolated tracks of the charged prongs, perpendicular to them, as shown in Figure (4.1).
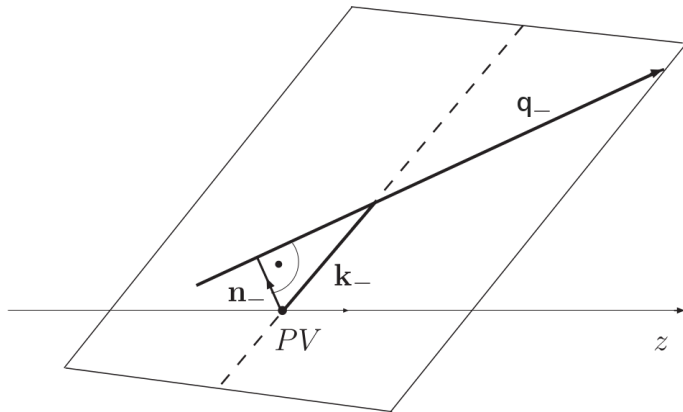

Figure 4.1.: Decay plane defined by the impact parameter n_- and the momentum q_- of a charged prong a^-. The τ^- momentum is labelled as k_- [32].

The figure above implies that one also needs to measure the 4-momenta $q_\pm^\mu = (E_\pm, q_\pm)$ of the charged prongs. Both the impact parameter vectors and the 4-momenta are measured in the laboratory frame. However, the sensitivity of the following relations turns out to be much higher in the $a^- \, a'^+$ ZMF. Therefore the momenta are boosted into this frame. The boosted vectors are labelled with an asterisk, for example $q_\pm^{*\mu}$. Since the true impact parameter in the charged prong ZMF can not be determined, one defines space-like impact parameter 4-vectors $n_\pm^\mu = (0, \hat{n}_\pm)$ in the laboratory frame. The spatial component of those vectors is filled with the normalised impact parameter vector. Eventually, $n_\pm^\mu$ also gets boosted in the $a^- \, a'^+$ ZMF. The resulting 4-vector is $n_\pm^{*\mu} = (n_{0\pm}^*, n_\pm^*)$. Subsequently, its 3-vector component gets split up in normalized constituents, which are either perpendicular or parallel to the corresponding, boosted 3-momentum $q_\pm^*$ [32]. This is shown in Equation (4.9):

$$n_\pm^* = n_\perp^{*\pm} + n_\parallel^{*\pm} = s \cdot \hat{n}_\perp^{*\pm} + t \cdot \hat{n}_\parallel^{*\pm}. \tag{4.9}$$

This is done because one needs to obtain an impact parameter which is perpendicular to the momentum, just like in the laboratory frame.

Finally, one has to normalise the boosted 3-momenta and then use some of the obtained vectors to define an angle φ^* ($0 \leq \varphi^* \leq \pi$):

$$\varphi^* = \arccos\left(\hat{n}_\perp^{*+} \cdot \hat{n}_\perp^{*-}\right), \tag{4.10}$$

and a CP-odd and T-odd correlation Θ_{CP}^* ($-1 \leq \Theta_{CP}^* \leq 1$):

$$\Theta_{CP}^* = \hat{q}_-^* \left(\hat{n}_\perp^{*+} \times \hat{n}_\perp^{*-} \right). \tag{4.11}$$

Last but not least, these two relations are used to define the signed angle between the $\tau^\pm \to a^\pm$ decay planes [30]

$$\varphi_{CP}^* = \begin{cases} \varphi^*, & \text{for } \Theta_{CP}^* \geq 0, \\ 2\pi - \varphi^*, & \text{for } \Theta_{CP}^* < 0. \end{cases} \tag{4.12}$$

The angle φ_{CP}^* ($0 \leq \varphi_{CP}^* \leq 2\pi$) and all the corresponding variables are visualised in Figure (4.2). In order to extract the CP mixing angle from the φ_{CP}^* distribution, a fit is performed using the following function:

$$f = u \cdot \cos \left(\varphi_{CP}^* - 2\phi_\tau' \right) + w. \tag{4.13}$$

Thereby, the amplitude u is required to be positive $u = |u|$. This way the function is forced to shift only via the angle ϕ_τ' and not via the sign of the cosine. The real mixing angle ϕ_τ is then obtained from the shift of the distribution with regards to the CP-even distribution, which is shifted by $\frac{\pi}{2}$. Consequently one gets:

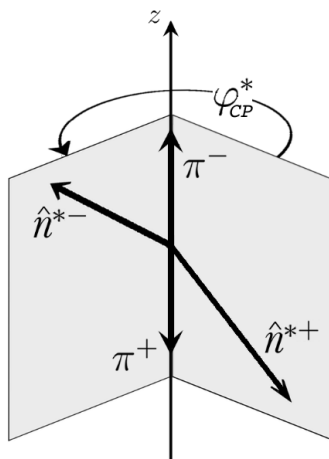$$\phi_\tau = \phi_\tau' - \frac{\pi}{2}. \tag{4.14}$$

Figure 4.2.: Visualisation of the angle φ_{CP}^* between the planes defined by the impact parameter vectors and 3-momenta of the charged prongs, which are, in this case, pions [1].

4.3. The ρ-decay plane method

As already mentioned, the ρ-decay plane method (RHO method) only covers the $\tau^+\tau^- \to \rho^+\rho^- + 2\,\nu_\tau$ decay mode. This method is implemented in the analyses in the same way it is described in [1]. If one aims to apply this method to data, it is important that both charged and both neutral pions from the ρ decays can be separated from each other. Additionally the momenta of the decay products must be measured and properly associated with the corresponding $\rho^\pm$ mesons. The momenta, which again define decay planes as shown in Figure (4.3), could be boosted into the $\rho^+\rho^-$ ZMF. However, in order to make the notation consistent with the impact parameter method, one rather boosts into the ZMF of the charged prongs, which are π^+ and π^- for the ρ decay. Later on, the combination of both methods simplifies this way.

After performing the boosts, one obtains the following spatial parts of the pion 4-momenta: $q^{*\pm}$, which describe the boosted momenta of the charged pions, and $q^{*0\pm}$, that denote the boosted momenta of the neutral pions assigned to the respective charged pions. Subsequently the $q^{*0\pm}$ vectors undergo the same procedure as introduced within the IP method: they get decomposed up into normalised, parallel and perpendicular components $\hat{q}_\perp^{*0\pm}$, $\hat{q}_\parallel^{*0\pm}$ with respect to the corresponding charged pion momenta. Analogously to the IP method the angle φ^* ($0 \le \varphi^* \le \pi$) is defined via:

$$\varphi^* = \arccos\left(\hat{q}_\perp^{*0+} \cdot \hat{q}_\perp^{*0-}\right). \tag{4.15}$$

The CP-odd correlation Θ_{CP}^* ($-1 \le \Theta_{CP}^* \le 1$) can by calculated using the following expression:

$$\Theta_{CP}^* = \hat{q}_-^*\left(\hat{q}_\perp^{*0+} \times \hat{q}_\perp^{*0-}\right). \tag{4.16}$$

This way the CP sensitive angle φ_{CP}^* does not need to be redefined and the expression in Equation (4.12) can be used for its calculation.

As described in [1, 33] one has to separate the events by the sign of the corresponding spin analysing function. Otherwise, the contributions from spin analysing powers with different signs would cancel out each other and the extracted angular distribution would remain flat. However, since the spin analysers in this channel are highly dependent[3] on the respective energy, one can divide the events by making use of the following energy relations:

$$y_+^\tau = \frac{(E_{\pi^+} - E_{\pi^0+})}{(E_{\pi^+} + E_{\pi^0+})} \quad \text{and} \quad y_-^\tau = \frac{(E_{\pi^-} - E_{\pi^0-})}{(E_{\pi^-} + E_{\pi^0-})}, \tag{4.17}$$

---

[3]In fact, the polarimeter vectors are proportional to $(E_{\pi^\pm} - E_{\pi^0\pm})$. Thereby, $E_{\pi^\pm}$ denotes the energy of the charged and $E_{\pi^0\pm}$ denotes the energy of the assigned neutral pion.

where all the energies are defined in the corresponding $\tau^{\pm}$ rest frames. One should multiply y_+^{τ} with y_-^{τ} to obtain

$$y^{\tau} = y_+^{\tau} \cdot y_-^{\tau}, \qquad (4.18)$$

and then select the events by the sign of y^{τ}, whereas, in a real world event selection one would rather separate by the energies in the laboratory frame, since the τ rest frame is not reconstructable with a satisfying precision. Thus, the following expressions will hold:

$$y_+^{L} = \frac{\left(E_{\pi+}^{L} - E_{\pi^0 +}^{L}\right)}{\left(E_{\pi+}^{L} + E_{\pi^0 +}^{L}\right)} \quad \text{and} \quad y_-^{L} = \frac{\left(E_{\pi-}^{L} - E_{\pi^0 -}^{L}\right)}{\left(E_{\pi-}^{L} + E_{\pi^0 -}^{L}\right)}, \qquad (4.19)$$

and finally select by the sign of y^{L}, whereby

$$y^{L} = y_+^{L} \cdot y_-^{L}. \qquad (4.20)$$

However, the amplitude of the distribution will decrease by cutting on y^{L} instead of y^{τ}.

Figure 4.3.: Visualisation of the angle φ_{CP}^{*} between the planes defined by the 3-momenta of the charged and the 3-momenta of the neutral pions [1].

4.4. The combination of the impact parameter method and the ρ-decay plane method

The combination of the impact parameter method and the ρ-decay plane method (IP-RHO method) covers the $\tau^+\tau^-$ decay modes, that see at least one τ lepton decaying into a $\rho^\pm$ meson. The other particle can decay via the channels given by the Equations (4.4) - (4.8). The method is adopted from [1].

The 4-momenta $q_\pm^\mu$ and $q_{0\pm}^\mu$ of the charged and neutral pions from the ρ decay have to be measured. One also needs access to the impact parameter vector $n_\mp$ and the 4-momentum $q_\mp^\mu$ of the charged prong $a^\mp$ from the decay of the second τ. Again, the impact parameter 4-vector gets defined as $n_\mp^\mu = (0, \hat{n}^\mp)$. As described in the previous methods, all 4-vectors then are boosted into the $a^\pm a'^\mp$ ZMF, where $a^\pm$ denotes the prong from the ρ decay. Subsequently, the boosted 3-vector parts $q^{*0\pm}$ and $n^{*\mp}$ get again decomposed into normalised, parallel and perpendicular components with respect to the momenta of the charged prongs.
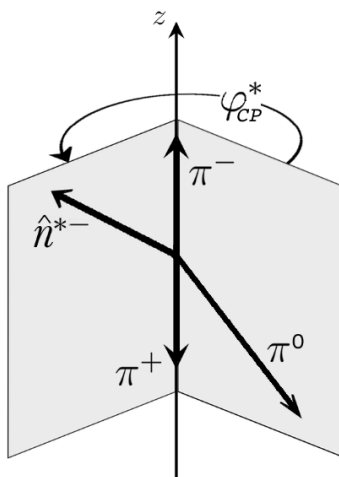
Figure 4.4.: Visualisation of the angle φ_{CP}^* between the planes defined by the 3-momentum and the impact parameter of the charged and the 3-momenta of the charged and neutral pions [1].

If one considers the decay mode $\tau^+\tau^- \to \rho^+ a^- + 2\nu_\tau \to \pi^+\pi^0 + X$, the angle φ^* and the triple correlation Θ_{CP}^* are calculated the following way:

$$\varphi^* = \arccos\left(\hat{q}_\perp^{*0+} \cdot \hat{n}_\perp^{*-}\right), \tag{4.21}$$

$$\Theta_{CP}^* = \hat{q}^{*-} \cdot \left(\hat{q}_\perp^{*0+} \times \hat{n}_\perp^{*-}\right). \tag{4.22}$$

4.4. The combination of the impact parameter method and the ρ-decay plane method

Again, the angle φ_{CP}^* can then be derived from Equation (4.12). One has to divide the events from $\tau^+ \to \rho^+$ by the sign of y_+^L, as described in Section (4.3). Even though not necessary for the decay modes $\tau^- \to \pi^-$ and $\tau^- \to a_1^{-\,L,T}$, one might split up the $\tau^- \to a^-$ depending on the sign of y_-^L as well, at least for the decay into a ρ^- meson. In this analysis the decay modes $\tau^\pm \to a^\pm$ are only split up for the decays, where $a^\pm = \rho^\pm$. The separation did not turn out to be very relevant for the decay $\tau^\pm \to a_1^\pm$.

If one considers the decay mode $\tau^+\tau^- \to \rho^- a^+ + 2\,\nu_\tau \to \pi^-\pi^0 + X$ the quantities of interest are calculated the following way:

$$\varphi^* = \arccos\left(\hat{q}_\perp^{*\,0-} \cdot \hat{n}_\perp^{*\,+}\right), \tag{4.23}$$

$$\Theta_{CP}^* = \hat{q}^{*\,-} \cdot \left(\hat{n}_\perp^{*\,+} \times \hat{q}_\perp^{*\,0-}\right). \tag{4.24}$$

The separation of events then proceeds analogously as explained above.

5. Results

Within this analyses, all the methods, described in the previous chapter, have been implemented in C++ code. The studies have been performed, based on Monte-Carlo generated data. In detail, the process $pp \to h \to \tau^+\tau^- + X$ was simulated at a COM energy of $\sqrt{s} = 13\,\text{TeV}$ by using the generator POWHEG and the parton shower simulator PYTHIA 8. The resulting data has been analysed using the xTAUFRAMEWORK, in order to obtain samples which contain all the relevant quantities for the analysis. Thereby, samples[1] for a CP-even and for a CP-odd Higgs boson have been considered. Unpolarised samples were used and reweighted with the xTAUSPINNER, in order to simulate a CP-mixed Higgs boson for different mixing angles. The xTAUSPINNER is a tool used by the xTAUFRAMEWORK to generate weights.

The most important Higgs production modes for the LHC, gluon-gluon-fusion (ggH) and vector-boson-fusion (VBF) have been studied. Additionally, the DRELL-YAN-background $Z \to \tau^+\tau^-$ was included in the analysis. The $\tau^+\tau^-$ system can either decay pure hadronically, semi-leptonically or pure leptonically. The pure hadronic decay mode (had-had) and the semi-leptonic case (lep-had) have been studied. The studies were performed on truth-level. In order to simulate uncertainty effects related to event reconstruction, a smearing was applied to the most relevant quantities.

5.1. Impact parameter method

The Figure (5.1) shows the fitted distribution of the angle φ_{CP}^*, for the decay mode $pp \to h \to \tau^+\tau^- \to \pi^+\pi^- + 2\,\nu_\tau$ (ggH), calculated using the impact parameter method. This channel has the maximal amplitude, since the spin analysing power is one for $\tau \to \pi$. A higher amplitude leads to less uncertainty in the CP mixing angle. Therefore channels with high amplitude are more relevant for the Higgs CP measurement than channels with a low amplitude. Figure (5.1) also contains the corresponding data points. However, for better clarity, the data points are not shown in most of the other plots.

For a better comparison of the φ_{CP}^*-distributions, it is useful to define the following

---

[1]The names of the used samples are listed at the end of appendix B.

5. Results

asymmetry coefficient[2] [1]:

$$A^{aa'} = \frac{1}{\sigma_{aa'}} \int_0^{2\pi} d\varphi_{CP}^* \left\{ d\sigma_{aa'} \left(u \cdot \cos\left(\varphi_{CP}^* - 2\,\phi_\tau' \right) > 0 \right) - d\sigma_{aa'} \left(u \cdot \cos\left(\varphi_{CP}^* - 2\,\phi_\tau' \right) < 0 \right) \right\}$$

$$= -\frac{4u}{2\pi w}, \tag{5.1}$$

where u is the amplitude and w the offset of the fitted function, see Equation (4.13). Since $A^{aa'}$ is a normalised value ($0 \le A^{aa'} \le 1$), it can be expressed in percent. The asymmetry does not depend on the mixing angle, but on the spin analysing powers. This becomes explicit, as the asymmetry can also be expressed via [30]:

$$A^{aa'} = \frac{\pi}{8} \frac{\int \, dE_{a'+} \, dE_{a-} \, n\left(E_{a'+} \right) \, n\left(E_{a-} \right) \, b\left(E_{a'+} \right) \, b\left(E_{a-} \right)}{\int \, dE_{a'+} \, dE_{a-} \, n\left(E_{a'+} \right) \, n\left(E_{a-} \right)}. \tag{5.2}$$
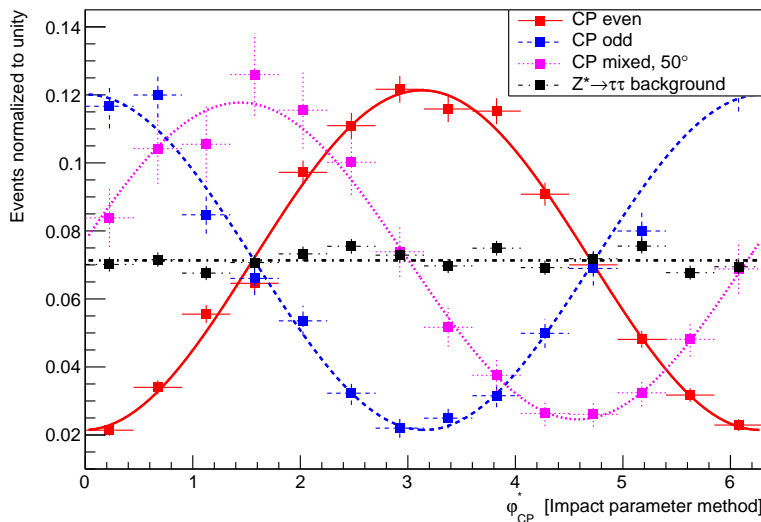
Figure 5.1.: Normalised φ_{CP}^* distributions for different CP mixing angles ϕ_τ of the Higgs boson h with $m_h = 125\,\text{GeV}$. The shown process is $pp \to h \to \tau^+\tau^- \to \pi^+\pi^- + 2\,\nu_\tau$. The cuts $p_T^{\pi^\pm} \ge 20\,\text{GeV}$ and $|\eta_{\pi^\pm}| \le 2.5$ have been applied.

The asymmetry calculated from plot reported in Figure (5.1) is roughly $44.5\,\%$ for the CP-even and odd case. The mixed sample shows a slightly decreased amplitude. This is due to the lack of statistics in this sample. The corresponding data points have larger errors, therefore the fit gets worse. All the respective fit parameters, the mixing angles ϕ_τ and the correlation matrices can be found in tables in the second appendix.

---

[2]The asymmetry coefficient is basically a normalised amplitude. A high asymmetry means a high amplitude and vice versa. Consequently, high asymmetries are desired to obtain a low uncertainty on the CP mixing angle.

The cuts $p_T^{\pi^\pm} \geq 20\,\text{GeV}$ and $|\eta_{\pi^\pm}| \leq 2.5$ were applied for the IP method. Rejecting charged prongs with a low p_T increases the amplitude, as shown in Figure (5.2). This behaviour is explained in detail in [30]: the differential partonic cross section for the process $i\,j \rightarrow h + X \rightarrow \tau^+ \tau^- + X \rightarrow a'^+ a^- + X$ at leading order is proportional to

$$1 + b\,(E_+)\,b\,(E_-)\,\left(\cos(\theta_+)\,\cos(\theta_-) - \sin(\theta_+)\,\sin(\theta_-)\,\cos(\varphi_{CP}^+ - 2\,\phi_\tau')\right), \qquad (5.3)$$

where $\theta_\pm = \angle(\hat{k}, \hat{q}_\pm)$ denote the polar angles of a'^+ and a^-, whereby $\hat{k}$ and $\hat{q}_\pm$ are, respectively, the directions of flight of the $\tau^\pm$ particles and the charged prongs. The angular distribution φ_{CP}^* arises from the last term in Equation (5.3). Cutting on the p_T of the charged prongs enhances the number of events, where $\cos(\theta_+)\,\cos(\theta_-) \approx 0$ and the contribution from the spin analysing powers gets stronger; therefore the asymmetry increases. In addition, a cut on the transverse momentum is unavoidable in order to suppress low-energy QCD background.
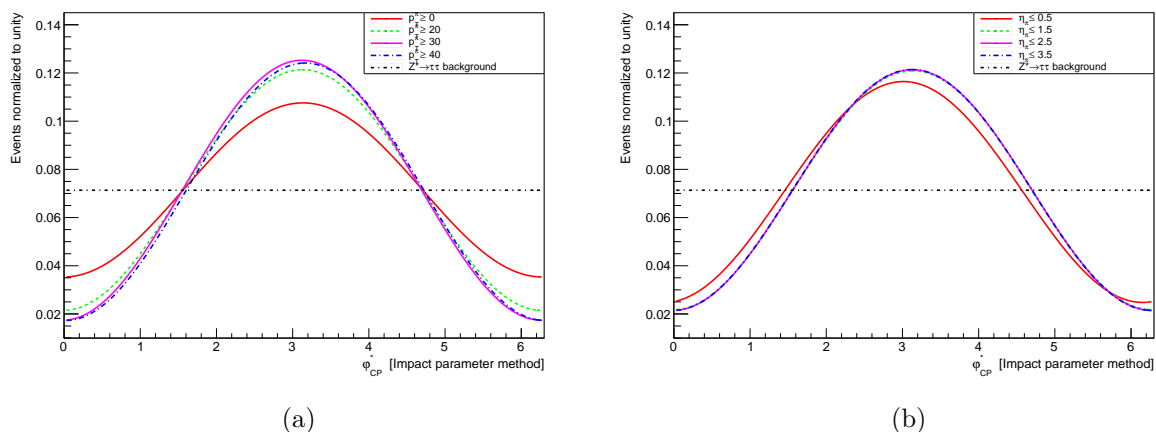

(a)   (b)

Figure 5.2.: Left: The normalised φ_{CP}^* distribution (CP-even, ggH) for different cuts on the transverse momentum ($p_T^{\pi^\pm} \geq 0$ (red), 20 (green), 30 (magenta), 40 GeV (blue)). The cut $|\eta_{\pi^\pm}| \leq 2.5$ was also applied. Right: The normalised φ_{CP}^* distribution for different cuts on the pseudorapidity ($|\eta_{\pi^\pm}| \leq 0.5$ (red), 1.5 (green), 2.5 (magenta), 3.5 (blue)). The cut $p_T^{\pi^\pm} \geq 20\,\text{GeV}$ was also applied.

The amplitude of the φ_{CP}^* distribution does not get affected by cuts on the pseudorapidity η, as shown in Figure (5.2). Indeed, in the case $|\eta| \leq 0.5$ one observes a shifted distribution, but this is due to the dramatic decrease of statistics that takes place if such a low $|\eta|$ cut is applied. However, the $|\eta_{\pi^\pm}| \leq 2.5$ cut is necessary since the high-η regions are not sufficiently covered by ATLAS. In fact, ATLAS also covers regions, where $|\eta| \geq 2.5$, but the quality of object reconstruction is lower with respect to the barrel region.

5. Results

In Figure (5.4), the impact of certain decay modes on the asymmetry is reported. Thereby, one observes the decay $\tau\tau \to \pi\, a_1^{L,T}$ to have the lowest asymmetry (7.5 %), even though the spin analysing power is maximal for this channel. However, since the transversal and longitudinal helicity states are not separated and their spin analysing functions have opposite signs, the amplitude remains low. The semi-leptonic decay mode $\tau\tau \to \pi\,\ell$ has an asymmetry of 16 %, whereby the spin analysing function of the lepton has a negative sign. Therefore the whole distribution gets shifted by $\varphi_{CP}^* \to \varphi_{CP}^* + \pi$, with respect to the CP-even distributions in the had-had case.
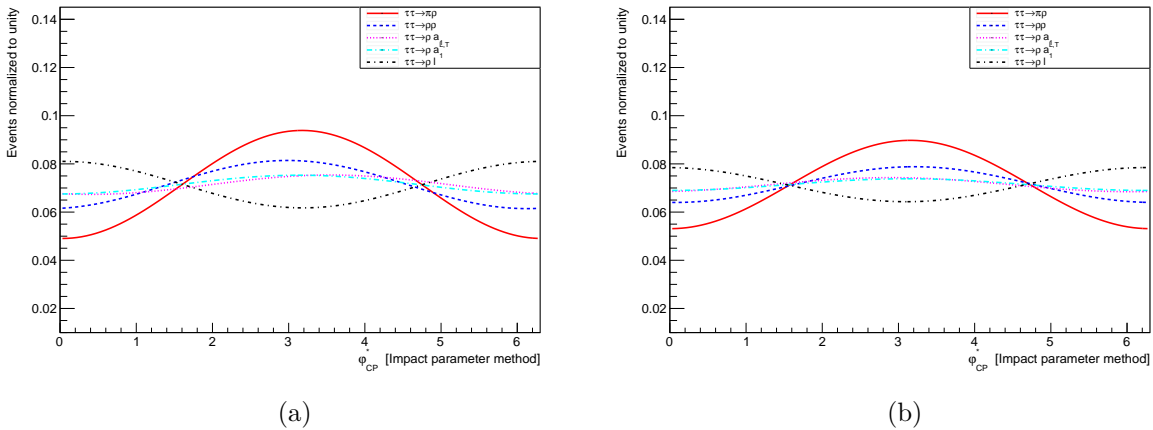

(a)   (b)

Figure 5.3.: Normalised φ_{CP}^* distributions for a CP-even Higgs boson h with $m_h = 125\,\mathrm{GeV}$ at the LHC for a COM of $13\,\mathrm{TeV}$. Different decay modes are shown, whereby at least one τ is required to decay into a ρ meson. The cuts $p_T^{\pi^\pm} \geq 20\,\mathrm{GeV}$ and $|\eta_{\pi^\pm}| \leq 2.5$ have been applied. Left: ggH events. Right: VBF events. Since the Higgs production mode is VBF, the asymmetries are smaller than in the ggH distributions on the left.

As expected, the same behaviour is also observed in the channels, where neither of both τ leptons decays into a single pion, see Figure (5.3). The asymmetry also depends on the production process, particularly, on the transverse momenta of the Higgs boson (the asymmetry will decrease for larger transverse momenta), as stated in [1, 32]. For instance, this effect can be seen on Figure (5.3), where the asymmetry is slightly decreased in the VBF samples.

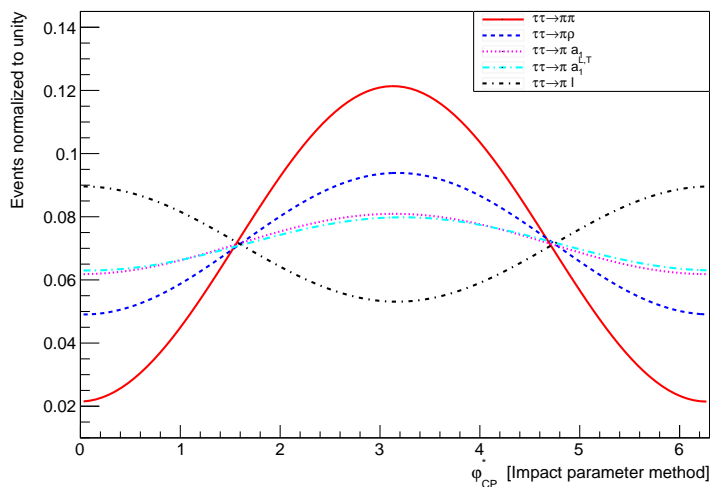In general, the background gives a flat φ_{CP}^* distribution, since the corresponding decays are unpolarised decays.

Figure 5.4.: The normalised φ^*_{CP} distribution (CP-even, ggH) for different decay modes, whereby one τ lepton decays into a single pion and the other decays in one of the possible channels. Applied cuts: $p_T^{\pi^\pm} \geq 20\,\text{GeV}$ and $|\eta_{\pi^\pm}| \leq 2.5$.

The φ^*_{CP} distributions were also calculated within the xTau Framework and compared to the results of this analyses. The code implemented into the xTau Framework and the code developed in this analysis are completely independent. Therefore, this analysis can also be used as a validation of the mentioned framework, which is used in data analysis. The comparison is reported in Figure (5.5) and it shows that both implementations match perfectly.
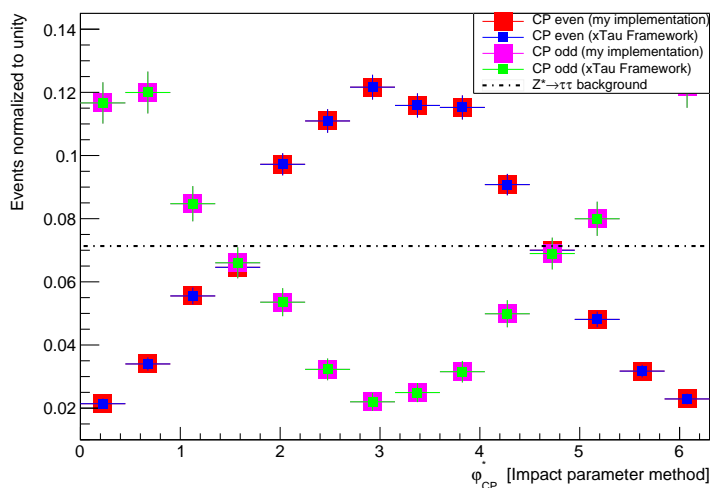

Figure 5.5.: Comparison between the normalised φ^*_{CP} distributions (CP-even and CP-odd, ggH), calculated with the xTau Framework (blue and green) and my own implementation (red and magenta). Applied cuts: $p_T^{\pi^\pm} \geq 20\,\text{GeV}$ and $|\eta_{\pi^\pm}| \leq 2.5$.

5. Results

One might wonder whether the angle φ^*, defined in Equation (4.10) shows sensitivity to the CP quantum number of the Higgs boson already in the laboratory frame or only in the charged prongs' ZMF. The answer on this question is given by Figure (5.6), which shows the distribution of φ^* in the laboratory frame. One can see that it is possible to distinguish between a CP-even and a CP-odd Higgs boson. However, this is only of academic interest, since the sensitivity is much lower than in the boosted frame.

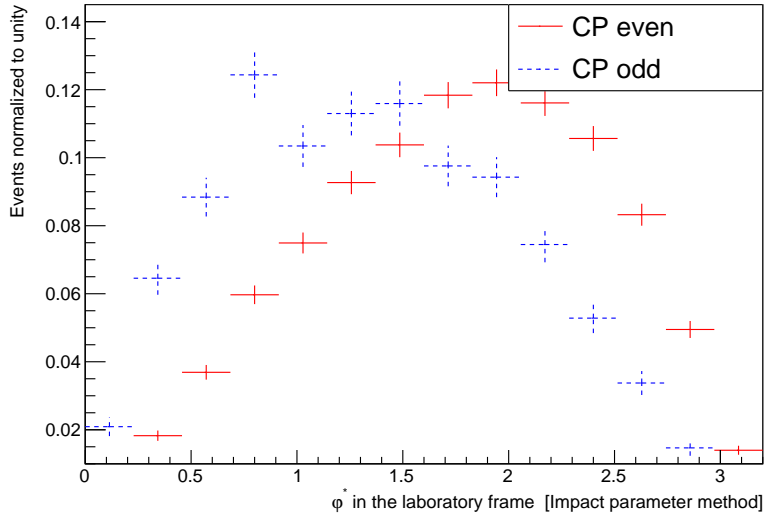**Figure 5.6.:** The normalised φ^* distribution in the laboratory frame for different CP quantum numbers (CP-even and CP-odd) of the Higgs boson h with $m_h = 125\,\text{GeV}$ at the LHC for a COM of $13\,\text{TeV}$ (ggH). The shown process is $pp \rightarrow h \rightarrow \tau^+\tau^- \rightarrow \pi^+\pi^- + 2\nu_\tau$. Applied cuts: $p_T^{\pi^\pm} \geq 20\,\text{GeV}$ and $|\eta_{\pi^\pm}| \leq 2.5$.

5.2. ρ-decay plane method

The Figure (5.7) shows the φ^*_{CP} distributions calculated using the ρ-decay plane method. Since the events are divided by the sign of y^τ, one gets two distributions, which are shifted by $\varphi^*_{CP} \to \varphi^*_{CP} + \pi$ with respect to each other. However, in order to make this method consistent with the IP method and also to increase the statistics, one rather shifts the $y^\tau < 0$ distribution back manually by $\varphi^*_{CP} \to \varphi^*_{CP} + \pi$. This way, both kind of events show the same modulation and can be added.

Figure 5.7.: Normalised φ^*_{CP} distributions for different CP mixing angles ϕ_τ. The shown process is $pp \to h \to \tau^+ \tau^- \to \rho^+ \rho^- + 2\,\nu_\tau$ (ggH). The cuts $p_T^{\rho^\pm} \geq 20\,\text{GeV}$ and $|\eta_{\rho^\pm}|$, $|\eta_{\pi^\pm}| \leq 2.5$ have been applied. Left: Events with $y^\tau > 0$. Right: Events with $y^\tau < 0$.

Figure (5.9) shows the impact of the quantity y on the φ^*_{CP} distributions, with respect to the chosen inertial frame of this variable. Additionally, the dependence on the transverse momenta is shown in this figure. By using y^τ, a cut of $p_T^{\rho^\pm} \geq 20\,\text{GeV}$ increases the asymmetry from $26.5\,\%$ to $26.7\,\%$. However in the lab frame (using y^L) the asymmetry is increased from $18\,\%$ to $20.5\,\%$ by cutting on the transverse momentum.

Again, the φ^*_{CP} distributions were also calculated with the XTAU FRAMEWORK for the CP-even and the CP-odd case. The comparison is shown in Figure (5.8). The results are compatible within the statistical uncertainty.
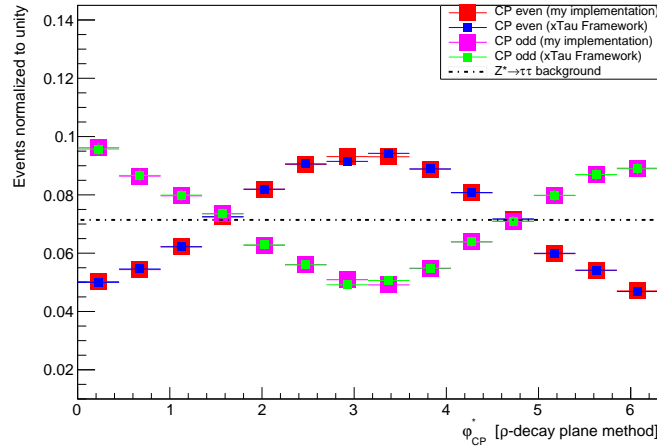
Figure 5.8.: Comparison between the normalised φ^*_{CP} distributions (CP-even and CP-odd, ggH), calculated with the XTAU FRAMEWORK (blue and green) and my own implementation (red and magenta) for the RHO method. In this distributions the events from $y^L < 0$ were already shifted back and added to the events with $y^L > 0$. Applied cuts: $p^{\rho^\pm}_T \geq 20\,\text{GeV}$ and $|\eta_{\rho^\pm}|$, $|\eta_{\pi^\pm}| \leq 2.5$.
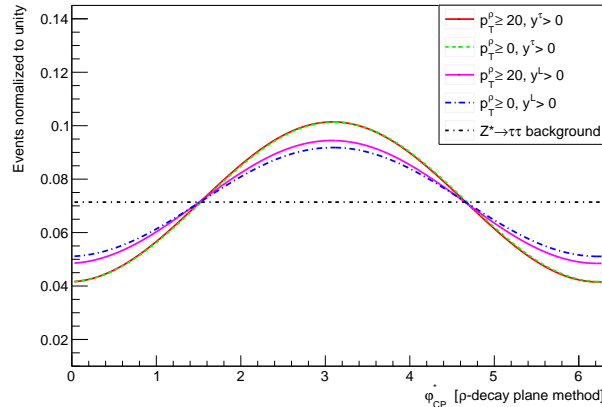
Figure 5.9.: The normalised φ^*_{CP} distributions with different combinations of cuts applied. The shown process is $pp \rightarrow h \rightarrow \tau^+\tau^- \rightarrow \rho^+\rho^- + 2\,\nu_\tau$ (CP-even, ggH). The cuts are $p^{\rho^\pm}_T \geq 20\,\text{GeV}$ or $p^{\rho^\pm}_T \geq 0\,\text{GeV}$ and $y^\tau > 0$ or $y^L > 0$. The cuts $|\eta_{\rho^\pm}|$, $|\eta_{\pi^\pm}| \leq 2.5$ have also been applied.

5.3. Combination of the IP and the RHO method

The impact parameter method and the ρ-decay plane method have been combined, as described in Chapter (4.4). The resulting φ^*_{CP} distributions for the process $\tau^+\tau^- \rightarrow \pi^\pm\rho^\mp$ are shown in Figure (5.10) for different CP mixing angles. The events were separated by

y^L. Again, for the further analyses the $y^L < 0$ events were shifted and added to the other events.
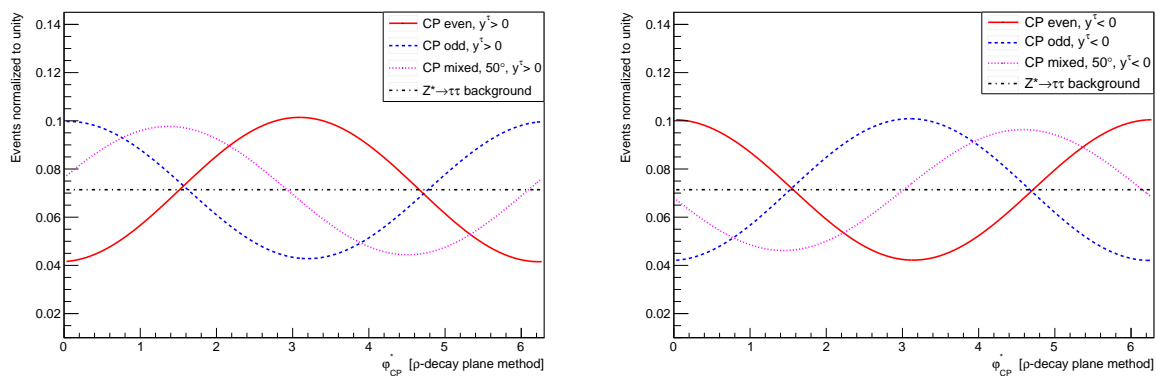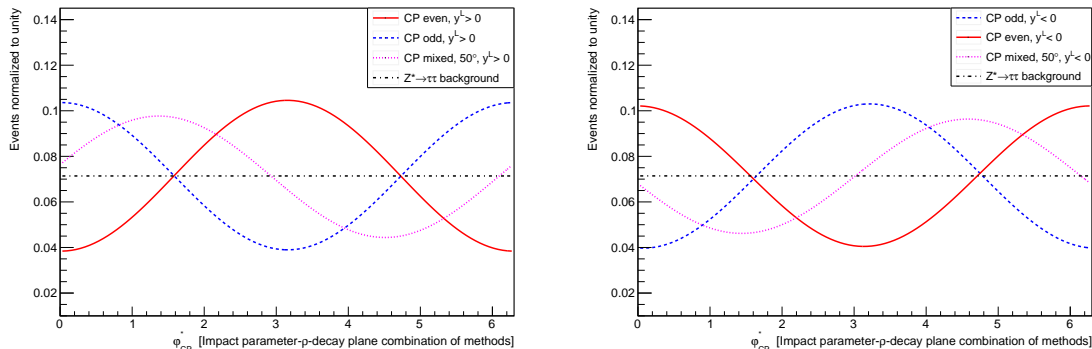

Figure 5.10.: Normalised φ^*_{CP} distributions for different CP mixing angles ϕ_τ. The shown process is $pp \rightarrow h \rightarrow \tau^+\tau^- \rightarrow \pi^\pm\rho^\mp + 2\nu_\tau$ (ggH). The cuts $p_T^{\pi^\pm}$, $p_T^{\rho^\mp} \geq 20\,\mathrm{GeV}$ and $|\eta_{\rho^\pm}|$, $|\eta_{\pi^\pm}| \leq 2.5$ have been applied. Left: Events with $y^L > 0$. Right: Events with $y^L < 0$.

The impact of the different decay modes on the φ^*_{CP} distribution for the IP-RHO method is shown in the appendix, Figure (A.1). The behaviour of the distributions is very similar to the IP method case. However their asymmetries are bigger, due to the fact that the IP-RHO method is more efficient than the IP method. A comparison between the two methods is shown in Figure (5.11).
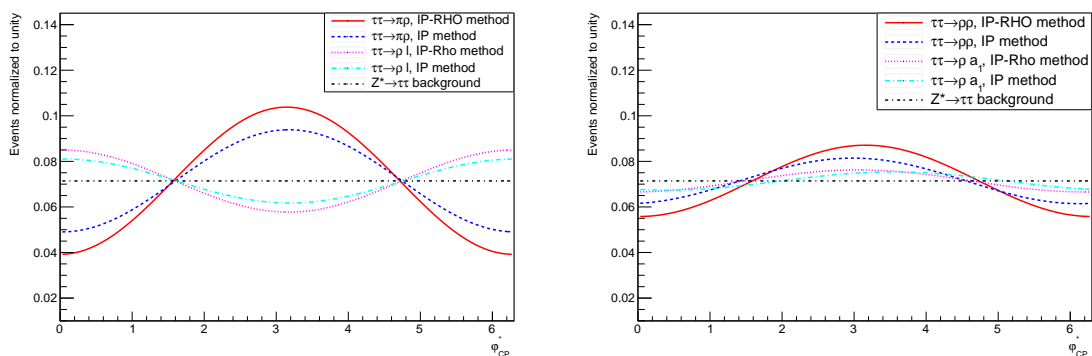
Figure 5.11.: Normalised φ^*_{CP} distributions for different decay modes and different methods (CP-even, ggH). The cuts $p_T^{\pi^\pm}$, $p_T^{\rho^\mp} \geq 20\,\mathrm{GeV}$ and $|\eta_{\rho^\pm}|$, $|\eta_{\pi^\pm}| \leq 2.5$ were applied. Left: The processes $\tau\tau \rightarrow \pi\rho$ and $\tau\tau \rightarrow \ell\,\rho$ are shown for the IP-RHO method (red and magenta), as well as for the IP method (blue and cyan). Right: The processes $\tau\tau \rightarrow \rho\rho$ and $\tau\tau \rightarrow \rho\,a_1$ are shown for the IP-RHO method (red and magenta), as well as for the IP method (blue and cyan).

5. Results

The calculated asymmetries differ, dependent on the respective decay mode. Using the IP-RHO method, one obtains an asymmetry of roughly 29 % in the $\tau\tau \to \pi\rho$ channel. The IP method gives an asymmetry of only 20 %. However, in the lep-had case the difference between both methods is smaller (12 % and 9 %). The same principle applies for the other decay modes, which are shown in the right plot on Figure (5.11).

Further, a comparison between all three methods was performed in the $\tau\tau \to \rho\rho$ channel. As expected the RHO method outperforms the other methods, whereby the IP method performs worst. The RHO method offers not only the highest asymmetry (20 %, IP-RHO method: 14 %, IP method: 9 %) but also the highest precision on the angle ($\Delta\phi_\tau = 0.5°$, IP-RHO method: 1°, IP method: 2.4°), as shown in Table (5.1). A full overview, including the plot and the corresponding fit parameters, is given in the appendix by Figure (A.2) and Table (B.6).

Method	Parameter	Name	Value	Error
RHO	CP-mixing angle	ϕ_τ	$-0.86°$	$0.49°$
	Asymmetry	$A^{aa'}$	$20.37\,\%$	$0.085\,\%$
IP-RHO	CP-mixing angle	ϕ_τ	$0.5°$	$1.04°$
	Asymmetry	$A^{aa'}$	$13.94\,\%$	$0.12\,\%$
IP	CP-mixing angle	ϕ_τ	$-4.52°$	$2.39°$
	Asymmetry	$A^{aa'}$	$8.9\,\%$	$0.19\,\%$

Table 5.1.: Comparison between the three different methods in the $\tau\tau \to \rho\rho$ channel.
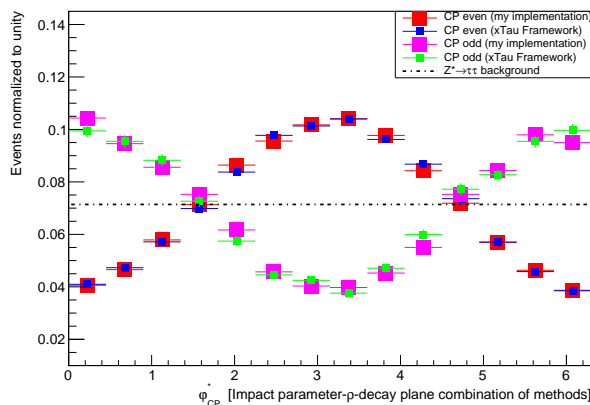
Figure 5.12.: Comparison between the normalised φ^*_{CP} distributions (CP-even and CP-odd, ggH), calculated with the xTau Framework (blue and green) and my own implementation (red and magenta) for the IP-RHO method. In this distributions the events from $y^L < 0$ were already shifted back and added to the events with $y^L > 0$. Applied cuts: $p_T^{\rho^\pm}$, $p_T^{\pi^\mp} \geq 20\,\text{GeV}$ and $|\eta_{\rho^\pm}|$, $|\eta_{\pi^\pm}| \leq 2.5$.

The comparison of the IP-RHO implementation with the xTau Framework is shown in Figure (5.12). In this respect again, the results are compatible within their statistical uncertainties.

5.4. Simulating detector uncertainties

Within this analysis, reconstruction uncertainties were studied for all the different methods and decay modes, as well as for all data samples, also including the $Z \rightarrow \tau\tau$ background.

In the case of the IP method, the uncertainties were simulated by applying a Gaussian smearing to the impact parameter vector components, as well as to the energy and the momenta of the charged prongs. Thereby, the impact parameters were smeared by 5 %. That means that the standard derivation σ of the Gaussian random number distribution is 5 % of the corresponding value of the impact parameter component. The same way the momenta got smeared by 3 % and the energies by 5 %. The impact of those simulated experimental uncertainties on the φ_{CP}^* distributions can be seen in Figure (5.13) for certain decay modes.
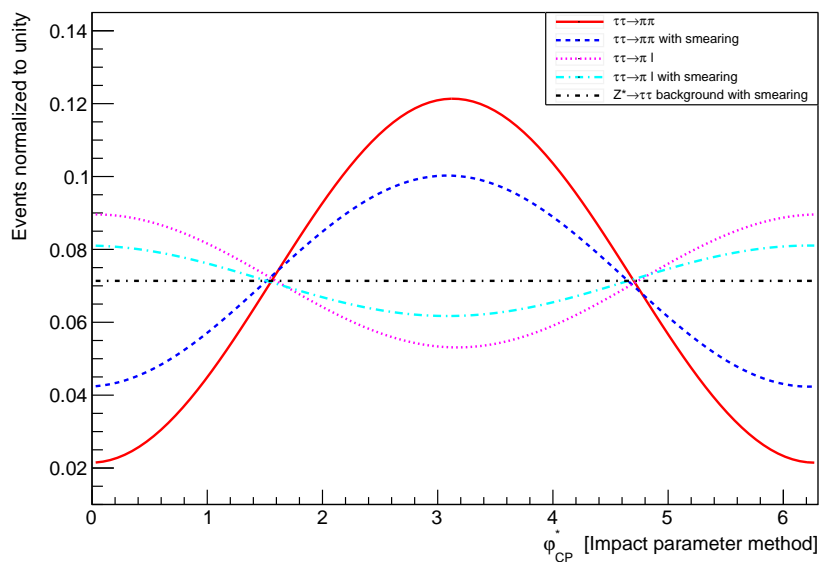
Figure 5.13.: Normalised φ_{CP}^* distributions for different decay modes and a CP-even Higgs boson with smearing applied (ggH). The cuts $p_T^{\pi^\pm} \geq 20\,\text{GeV}$ and $|\eta_{\pi^\pm}| \leq 2.5$ were applied.

5. Results

The smeared distributions not only give less asymmetry respecting to corresponding un-smeared distributions (from $44.5\,\%$ to $26\,\%$ for $\tau\tau \to \pi\pi$ and from $16\,\%$ to $9\,\%$ for $\tau\tau \to \pi\,\ell$), but are also slightly shifted, which is even a bigger problem in a real data analyses, since such shifts distort the true value of the CP mixing angle.
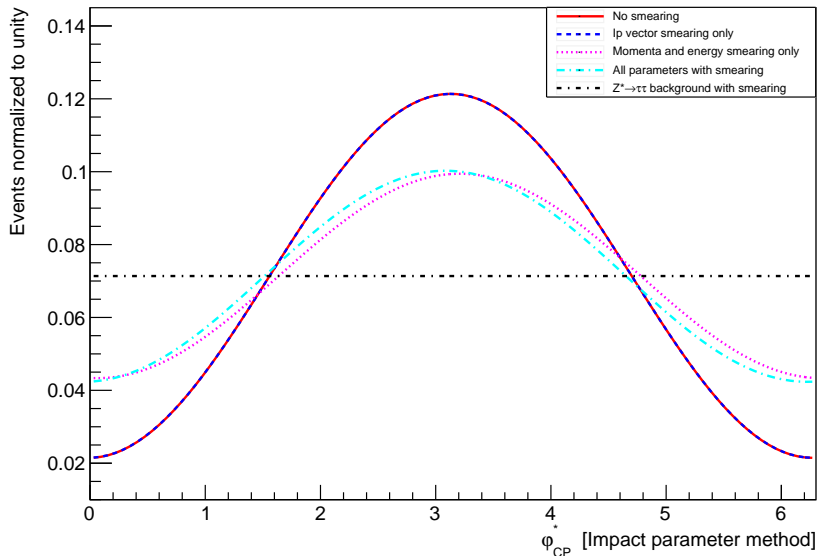
Figure 5.14.: Normalised φ_{CP}^* distributions for the decay mode $\tau\tau \to \pi\pi$ and a CP-even Higgs boson (ggH). Red line: no smearing applied. Blue line: only the impact parameters got smeared. Magenta line: only the energies and momenta were smeared. Cyan line: All parameters were smeared. The cuts $p_T^{\pi^\pm} \geq 20\,\text{GeV}$ and $|\eta_{\pi^\pm}| \leq 2.5$ were applied.

Besides, the Figure (5.14) shows what happens if only the impact parameter or only the momentum and energy gets smeared. In the first case, the smearing does not seem to affect the distribution. However, this no longer holds if the momentum and energy uncertainties are also considered. Those let the asymmetry drop by roughly $20\,\%$. The uncertainty on the impact parameter then slightly shifts the distribution.

For the RHO method, the charged pions' momenta are smeared by $3\,\%$ and their energies by $5\,\%$, whereas the neutral pions' momenta are smeared by $6\,\%$ and their energies by $10\,\%$. The resulting distributions are shown in Figure (5.15).
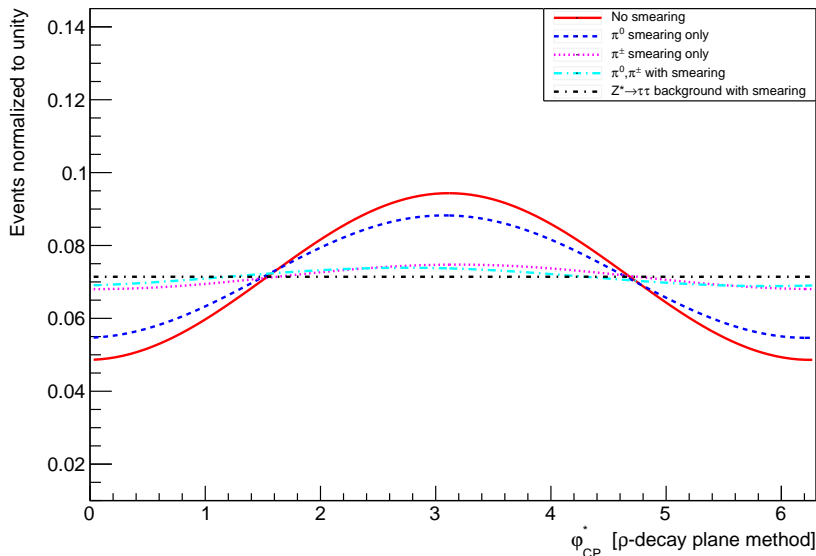
Figure 5.15.: Normalised φ^*_{CP} distributions for the decay mode $\tau\tau \to \rho\rho$ and a CP-even Higgs boson with smearing applied (ggH). The red line shows the distribution with no smearing applied. The distribution, where only the π^0 parameters got smeared, is shown in blue. The distribution, where only the $\pi^\pm$ parameters got smeared, is shown in magenta. All parameters were smeared in the cyan distribution. The cuts $p_T^{\rho^\mp} \geq 20\,\text{GeV}$ and $|\eta_{\rho^\pm}|,\ |\eta_{\pi^\pm}| \leq 2.5$ were applied.

The smearing of the charged pion has a much larger impact on the distribution than the smearing of the neutral pion. This effect is expected [1] and it mainly due to the distorted ZMF of the charged particles. It was already shown in the previous chapters that the φ^*_{CP} distribution is very sensitive to the chosen inertial frame. The same effect, even though with less impact, is also visible in the distributions calculated with IP-RHO method, see appendix. The effect is less strong, since only one τ lepton decays into a ρ meson. The ρ decay modes seem to get strongly affected by smearing.

For the IP-RHO method, the parameters got smeared to the same amount as in the RHO method. However, since the impact parameter vector is used in the IP-RHO method, 5 % smearing was also applied to this quantity.

5.5. Combination of different decay modes and estimation of the achievable precision on ϕ_τ

The achievable precision on the Higgs CP mixing angle is of major interest. On truth-level, the decay modes with a high asymmetry show an error under $1\,\%$ on ϕ_τ throughout all methods. Thereby, the uncertainty is taken from the fit applied to the distribution. The channels with lower asymmetry usually show slightly larger errors, but this is mainly due to the decrease of statistics in these channels. However, with real data analyses in mind, one would like to have the maximum possible statistics since the signal is distorted by measurement uncertainties and dominated by background. Therefore it is convenient not to use a single CP analysing method, but rather using all methods among each other. One possible combination of the methods is to use the RHO method for the channel, where both τ leptons decay into ρ mesons, the IP-RHO method for the modes, where only one τ decays into a ρ and eventually the IP method is used for the remaining channels. The resulting distributions are then added together and a single fit is performed. This arrangement of methods will be called "Standard combination of methods" within this analysis. A second approach is to use all methods for all channels[3]. This will be called "Alternative combination of methods". Further it is also possible to choose only the channels with the highest asymmetry (for instance the ten best or the five best) and reject the other channels with lower asymmetry.

Instead of combining the decay channels and performing the fit afterwards, one can also fit simultaneously over all decay channels, or a selection of the best channels, and taking the weighted mean of the obtained mixing angles.

The principle of these different possibilities is reported in Table (5.2) for a CP-even had-had sample (ggH) with smearing applied.

Combination of methods	Asymmetry	ϕ_τ	$\Delta\phi_\tau$	Expected Value
Standard	$4.5\,\%$	$-3.48°$	$1.39°$	$0°$
Alternative	$4.9\,\%$	$-2.78°$	$1.13°$	$0°$
Alternative (full)	$3.7\,\%$	$-2.49°$	$1.24°$	$0°$
Top five	$6.6\,\%$	$-2.53°$	$1.1°$	$0°$
Top five (simultaneous fit)	$-$	$-1.7°$	$0.83°$	$0°$

Table 5.2.: Comparison between different combinations of methods for a CP-even had-had sample (ggH) with smearing applied.

---

[3]Of course only the channels, they are compatible with. For instance, it does not make sense to apply the RHO method to a single pion decay.

5.5. Combination of different decay modes and estimation of the achievable precision on ϕ_τ

From the results in the table, the Standard combination of methods gives the worst performance. The alternative approach works better, even in the "full" case, which means that all decay channels of the sample are analysed, including for instance those decays that have three charged prongs and one or more neutral pion. These were not included in Equation (4.4) - (4.8). However, the alternative combination works even better with those modes rejected. The most interesting combination is probably the simultaneous fit, which was in this case performed on the top five decay modes. With respect to the Standard combination of methods, the value of the mixing angle is more than two times closer at the expected value. Even more important, the error of the angle is reduced by the factor 1.67. One could even improve the errorbars further by including more channels (top ten for example), but the actual value of ϕ_τ might suffer from this approach, since one would add contributions which are, for statistical reasons, less close to the expected value.

As a final study, the ggH, VBF and $Z \to \tau\tau$ background samples were combined together in order to give an estimation on the achievable precision on ϕ_τ. However, the lep-had and had-had samples remained separately and were not added. Smearing was applied. The different samples were scaled with respect to the sample luminosity of the ggH sample, which is $120 \, \text{fb}^{-1}$. The signal to background ratio was $6.8 \cdot 10^{-3}$. The results for the signal plus background distributions are shown for the had-had case in Table (5.3).

Combination of methods	Asymmetry	ϕ_τ	$\Delta\phi_\tau$	Expected Value
Standard	0.24 %	−4.38°	20.86°	0°
Alternative	0.27 %	−6.64°	16.62°	0°
Top five	0.43 %	−50.45°	13.26°	0°

Table 5.3.: Comparison between different combinations of methods for the signal (ggH and VBF) plus background ($Z \to \tau\tau$) distribution with smearing applied.

Again, the alternative combination of methods outperforms the standard combination in terms of $\Delta\phi_\tau$. Although it has the smallest errors, the top-five-combination suffers from a ϕ_τ value which is quite far from the expected value. Simultaneous fits on the signal plus background combinations were not performed within this analysis.

6. Discussion and outlook

Within this analysis, all the methods described in [1] and all the corresponding plots have been re-obtained. The Figure (5.6) is consistent with the plot shown in [32].

Although all the calculated asymmetries are a bit lower than shown in [1], they lie in the same order of magnitude. Anyway, the asymmetries should not be considered as a fixed quantity. They strongly depend on the quality of the fit. Therefore, statistical quantities such as the binning of the histograms can change the asymmetry. In all plots of this analyses 14 bins were used. Initially only seven bins were used, and a decrease in the asymmetry by about 1% with respect to the same histograms with 14 bins was observed. All major decay modes have been studied and they show the behaviour expected from [1, 30]. However, in a future analyses one should definitely study the effect of a separation of the longitudinal helicity states from the $a_1^{L,T}$ resonance on the φ_{CP}^* distribution. Since this decay channel has a maximal spin analysing power, a higher asymmetry should be expected. If the corresponding distributions indeed had a high amplitude when separated properly, the channel could become very relevant, in particular with a view to the achievable precision on the mixing angle ϕ_τ.

The effects of measurement uncertainties were studied and the results are consistent with [1]. The estimation of the angle uncertainty is given in the respective article with $\Delta\phi_\tau = 15°$ for a luminosity of $150\,\mathrm{fb}^{-1}$ (Standard combination of methods). This seems to be consistent with $\Delta\phi_\tau = 21°$ for a luminosity of $120\,\mathrm{fb}^{-1}$. One should note that they obtain an asymmetry of 8.1% for the had-had case. The asymmetry calculated within this analyses is considerably lower (0.24%). However they are assuming a signal to background ratio of 1, while a S/B ratio of $6.8 \cdot 10^{-3}$ was assumed in this analyses. This ratio was calculated from the total cross sections and luminosities of the respective samples and seems to be much more realistic than a value of 1. One should also keep in mind that way of applying the smearing effects was different in [1]. For example, the impact parameter vector got smeared by applying smearing to the corresponding vertices. In this analysis the vector components got smeared directly. However, as mentioned above the impact of the uncertainties are still very similar.

In a future analysis, one should definitely consider simultaneous fitting over all decay

modes (for the signal plus background distributions). The positive effect of this way of fitting was demonstrated and could lead to a much better angular resolution. Further, reconstruction-level studies are the next logical step in order to estimate detector effects. The implemented methods in the xTau Framework were cross checked and validated within this thesis. However, one might investigate further where the small differences between both implementations, that one can observe for the RHO and the IP-RHO method, arise from.

A. First appendix
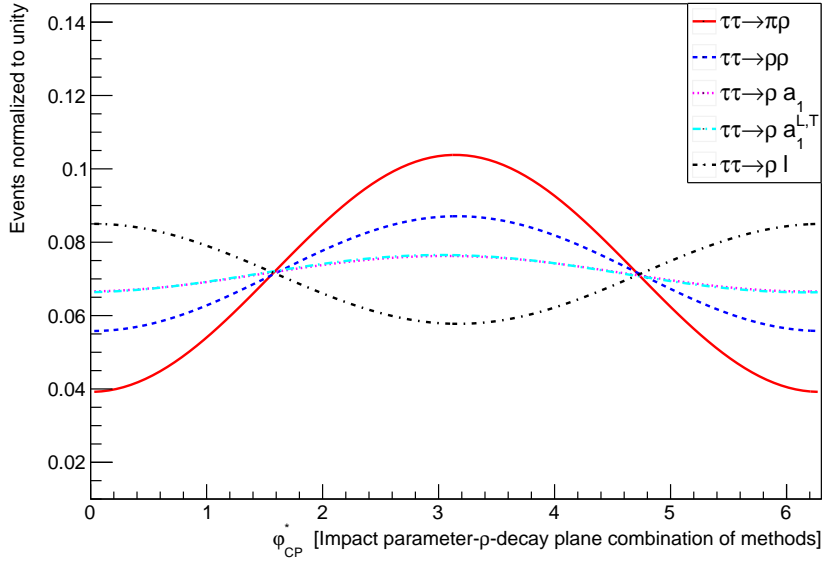
Figure A.1.: Normalised φ_{CP}^{*} distributions for a CP-even Higgs boson h with $m_h = 125\,\mathrm{GeV}$ at the Lʜᴄ for a COM of $13\,\mathrm{TeV}$ (ggH). Distributions for different decay modes are shown, calculated with the IP-RHO method. The cuts $p_T^{\rho^{\mp}}$, $p_T^{\pi^{\mp}} \geq 20\,\mathrm{GeV}$ and $|\eta_{\rho^{\pm}}|$, $|\eta_{\pi^{\pm}}| \leq 2.5$ have been applied.
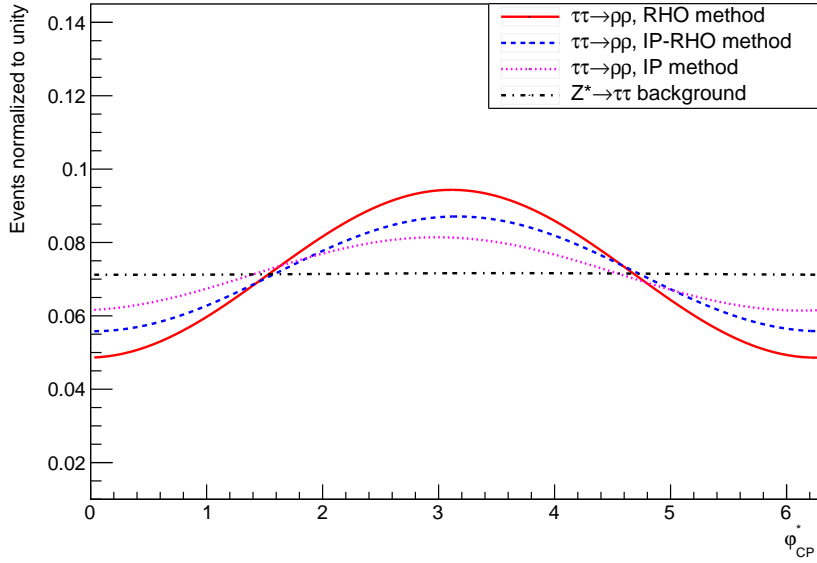
Figure A.2.: Comparison between the normalised φ_{CP}^* distributions, calculated by the three different methods for a CP-even Higgs boson (ggH). The process is $pp \to h \to \tau^+\tau^- \to \rho^+\rho^- + 2\,\nu_\tau$. The respective methods' usual cuts were applied to each distribution.
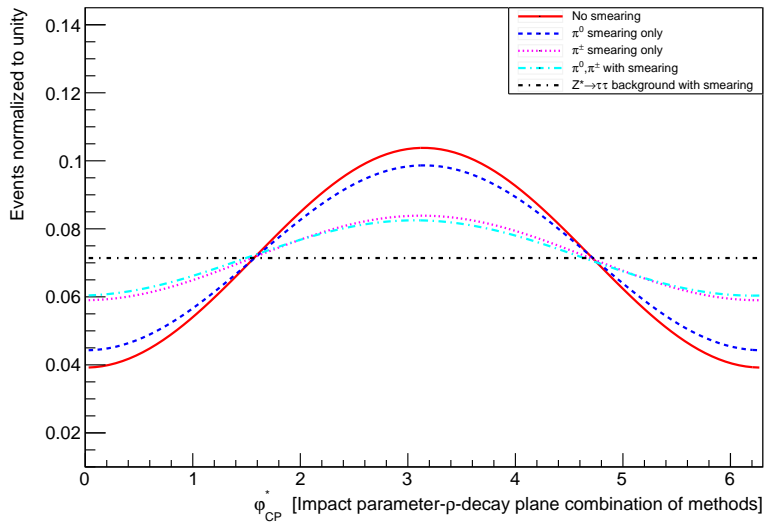
Figure A.3.: Normalised φ_{CP}^* distributions for the decay mode $\tau\tau \to \pi\rho$ and a CP-even Higgs boson with smearing applied (ggH). The red line shows the distribution with no smearing applied. The distribution, where only the π^0 parameters got smeared, is shown in blue. The distribution, where only the $\pi^\pm$ parameters got smeared, is shown in magenta. All parameters were smeared in the cyan distribution. The cuts $p_T^{\pi^\pm}$, $p_T^{\rho^\mp} \geq 20\,\text{GeV}$ and $|\eta_{\rho^\pm}|$, $|\eta_{\pi^\pm}| \leq 2.5$ were applied.

B. Second appendix

The Table (B.1) shows the fit parameters and the CP mixing angles for the plot shown in Figure (5.1).

Sample	Parameter	Name	Value	Error	Exp. Value[1]
CP-even	Amplitude	u	0.0499439	0.00104631	
	Offset	w	0.0714149	0.000802239	
	CP-mixing angle	ϕ_τ	$-0.335638°$	$0.603903°$	$0°$
	Asymmetry	$A^{aa'}$	$44.5219\,\%$	$0.20177\,\%$	$50\,\%$
	Goodness of the fit	$\chi^2/\text{d.o.f}$	1.4968		
CP-odd	Amplitude	u	0.0493216	0.00179491	
	Offset	w	0.0707817	0.00136059	
	CP-mixing angle	ϕ_τ	$-89.6686°$	$1.03079°$	$\pm 90°$
	Asymmetry	$A^{aa'}$	$44.3604\,\%$	$0.351743\,\%$	$50\,\%$
	Goodness of the fit	$\chi^2/\text{d.o.f}$	1.78356		
CP-mixed	Amplitude	u	0.0465781	0.00274917	
	Offset	w	0.0711642	0.0021172	
	CP-mixing angle	ϕ_τ	$-48.7308°$	$1.49213°$	$\pm 50°$
	Asymmetry	$A^{aa'}$	$41.6677\,\%$	$0.501384\,\%$	$50\,\%$
	Goodness of the fit	$\chi^2/\text{d.o.f}$	0.221687		

Table B.1.: Fit parameters.

The Table (B.5) shows the corresponding correlations matrices for the fits shown in Table (B.1). These kind of matrices will be shown here once, since they should only motivate the error calculation for the asymmetry $A^{aa'}$. One can see in the correlation matrices that the parameters u and w are sometimes more correlated and sometimes less. To meet this correlation, the respective covariances are considered in the error formula of the

---

[1]The expected Value. For the CP mixing angle the expected value is explicitly defined. However, in the case of the asymmetries, the values from [1] are shown (if available). However, these values are systematically higher than those calculated within this thesis. Therefore they should just be taken as an expected order of magnitude.

B. Second appendix

asymmetry:

$$\sigma_{A^{aa'}} = |A^{aa'}| \cdot \sqrt{\left(\frac{\sigma_u}{4u}\right)^2 + \left(\frac{\sigma_w}{2\pi w}\right)^2 - 2\left(\frac{\sigma_{uw}}{8\pi uw}\right)}. \tag{B.1}$$

In Table (B.2) the fit parameters and CP mixing angles are shown for different decay modes, calculated with the impact parameter method. The corresponding plot is given in Figure (5.4).

Mode	Parameter	Name	Value	Error	Exp. Value
$\tau\tau \to \pi\pi$	Amplitude	u	0.0499439	0.00104631	
	Offset	w	0.0714149	0.000802239	
	CP-mixing angle	ϕ_τ	$-0.335638°$	$0.603903°$	$0°$
	Asymmetry	$A^{aa'}$	$44.5219\,\%$	$0.20177\,\%$	$50\,\%$
	Goodness of the fit	$\chi^2/\text{d.o.f}$	1.4968		
$\tau\tau \to \pi\rho$	Amplitude	u	0.022413	0.000655565	
	Offset	w	0.0714669	0.00047193	
	CP-mixing angle	ϕ_τ	$0.929039°$	$0.845928°$	$0°$
	Asymmetry	$A^{aa'}$	$19.9652\,\%$	$0.142651\,\%$	
	Goodness of the fit	$\chi^2/\text{d.o.f}$	0.640988		
$\tau\tau \to \pi\,a_1$	Amplitude	u	0.00955426	0.00113235	
	Offset	w	0.071374	0.000805776	
	CP-mixing angle	ϕ_τ	$0.0460434°$	$3.42192°$	$0°$
	Asymmetry	$A^{aa'}$	$8.52192\,\%$	$0.251446\,\%$	
	Goodness of the fit	$\chi^2/\text{d.o.f}$	0.803167		
$\tau\tau \to \pi\,a_1^{L,T}$	Amplitude	u	0.00841451	0.000658177	
	Offset	w	0.0714088	0.000468843	
	CP-mixing angle	ϕ_τ	$2.4028°$	$2.26558°$	$0°$
	Asymmetry	$A^{aa'}$	$7.50166\,\%$	$0.146215\,\%$	
	Goodness of the fit	$\chi^2/\text{d.o.f}$	1.24918		
$\tau\tau \to \pi\,\ell$	Amplitude	u	0.0182495	0.000469027	
	Offset	w	0.0713512	0.000334018	
	CP-mixing angle	ϕ_τ	$90.7591°$	$0.734933°$	$\pm 90°$
	Asymmetry	$A^{aa'}$	$16.2828\,\%$	$0.103148\,\%$	
	Goodness of the fit	$\chi^2/\text{d.o.f}$	1.64461		

Table B.2.: Fit parameters.

The Table (B.3) shows the fit parameters and CP mixing angles for different cuts, calculated with the ρ-decay plane method (see Figure (5.9)).

Cuts	Parameter	Name	Value	Error	Exp. Value
$p_T^\rho \geq 20\,\text{GeV}$ $y^\tau > 0$	Amplitude	u	0.029949	0.000545655	
	Offset	w	0.0714695	0.000396713	
	CP-mixing angle	ϕ_τ	$-1.5141°$	$0.525839°$	$0°$
	Asymmetry	$A^{aa'}$	$26.6773\,\%$	$0.116432\,\%$	$29\,\%$
	Goodness of the fit	$\chi^2/\text{d.o.f}$	1.63102		
$p_T^\rho \geq 0\,\text{GeV}$ $y^\tau > 0$	Amplitude	u	0.0298478	0.000488995	
	Offset	w	0.0714857	0.00035542	
	CP-mixing angle	ϕ_τ	$-1.02859°$	$0.472733°$	$0°$
	Asymmetry	$A^{aa'}$	$26.5811\,\%$	$0.104354\,\%$	$28\,\%$
	Goodness of the fit	$\chi^2/\text{d.o.f}$	1.19282		
$p_T^\rho \geq 20\,\text{GeV}$ $y^L > 0$	Amplitude	u	0.0229962	0.000553314	
	Offset	w	0.0714591	0.000398038	
	CP-mixing angle	ϕ_τ	$-1.81362°$	$0.693864°$	$0°$
	Asymmetry	$A^{aa'}$	$20.487\,\%$	$0.120269\,\%$	$21\,\%$
	Goodness of the fit	$\chi^2/\text{d.o.f}$	1.27889		
$p_T^\rho \geq 0\,\text{GeV}$ $y^L > 0$	Amplitude	u	0.0203748	0.000496863	
	Offset	w	0.0714509	0.000356165	
	CP-mixing angle	ϕ_τ	$-1.49446°$	$0.702515°$	$0°$
	Asymmetry	$A^{aa'}$	$18.1537\,\%$	$0.108597\,\%$	$14\,\%$
	Goodness of the fit	$\chi^2/\text{d.o.f}$	1.65981		

Table B.3.: Fit parameters.

The Table (B.4) shows the fit parameters and CP mixing angles for different decay modes calculated either with the IP or IP-RHO method. The corresponding plot is given by Figure (5.11).

Mode	Parameter	Name	Value	Error	Exp. Value
IP-RHO mehtod $\tau\tau \to \pi\rho$	Amplitude	u	0.032301	0.000444351	
	Offset	w	0.0715053	0.000323987	
	CP-mixing angle	ϕ_τ	0.0290579°	0.395954°	0°
	Asymmetry	$A^{aa'}$	28.7579 %	0.0940598 %	36 %
	Goodness of the fit	$\chi^2/\text{d.o.f}$	0.628163		
IP mehtod $\tau\tau \to \pi\rho$	Amplitude	u	0.022413	0.000655565	
	Offset	w	0.0714669	0.00047193	
	CP-mixing angle	ϕ_τ	0.929034°	0.845927°	0°
	Asymmetry	$A^{aa'}$	19.9653 %	0.142651 %	
	Goodness of the fit	$\chi^2/\text{d.o.f}$	0.640988		
IP-RHO mehtod $\tau\tau \to \pi\ell$	Amplitude	u	0.0136282	0.000296905	
	Offset	w	0.0713788	0.000211274	
	CP-mixing angle	ϕ_τ	90.7803°	0.626578°	±90°
	Asymmetry	$A^{aa'}$	12.1548 %	0.0656906 %	
	Goodness of the fit	$\chi^2/\text{d.o.f}$	1.90285		
IP mehtod $\tau\tau \to \pi\ell$	Amplitude	u	0.00964603	0.0004459	
	Offset	w	0.0713929	0.000316719	
	CP-mixing angle	ϕ_τ	91.2814°	1.33061°	±90°
	Asymmetry	$A^{aa'}$	8.60149 %	0.0990286 %	
	Goodness of the fit	$\chi^2/\text{d.o.f}$	0.628946		

Table B.4.: Fit parameters.

Sample		u	ϕ_τ	w
CP-even	u	1	0.00177425	0.538708
	ϕ_τ	0.00177425	1	$5.45153e-05$
	w	0.538708	$5.45153e-05$	1
CP-odd	u	1	0.0022293	0.525639
	ϕ_τ	0.0022293	1	$-3.63177e-05$
	w	0.525639	$-3.63177e-05$	1
CP-mixed	u	1	-0.00183698	0.682432
	ϕ_τ	-0.00183698	1	0.00429506
	w	0.682432	0.00429506	1

Table B.5.: Correlation matrices.

The Table (B.6) shows the fit parameters and CP mixing angles for the decay $\tau\tau \to \rho\rho$, calculated with all three different methods. The corresponding plot is given by Figure (A.2).

Method	Parameter	Name	Value	Error	Exp. Value
RHO	Amplitude	u	0.0228739	0.000389204	
	Offset	w	0.0714784	0.000279771	
	CP-mixing angle	ϕ_τ	$-0.862323°$	$0.490088°$	$0°$
	Asymmetry	$A^{aa'}$	$20.3725\,\%$	$0.0846012\,\%$	$21\,\%$
	Goodness of the fit	$\chi^2/$d.o.f	0.967602		
IP-RHO	Amplitude	u	0.0156458	0.00056293	
	Offset	w	0.0714461	0.000402287	
	CP-mixing angle	ϕ_τ	$0.49631°$	$1.03944°$	$0°$
	Asymmetry	$A^{aa'}$	$13.9411\,\%$	$0.124013\,\%$	
	Goodness of the fit	$\chi^2/$d.o.f	0.987419		
IP	Amplitude	u	0.00999489	0.000834978	
	Offset	w	0.0714287	0.000591932	
	CP-mixing angle	ϕ_τ	$-4.51797°$	$2.3928°$	$0°$
	Asymmetry	$A^{aa'}$	$8.9081\,\%$	$0.185207\,\%$	
	Goodness of the fit	$\chi^2/$d.o.f	0.48556		

Table B.6.: Fit parameters.

Mode	Parameter	Name	Value	Error	Exp. Value
No smearing $\tau\tau \to \pi\pi$	Amplitude	u	0.0499439	0.00104631	
	Offset	w	0.0714149	0.000802239	
	CP-mixing angle	ϕ_τ	$-0.335638°$	$0.603903°$	$0°$
	Asymmetry	$A^{aa'}$	$44.5219\,\%$	$0.20177\,\%$	$50\,\%$
	Goodness of the fit	$\chi^2/$d.o.f	1.4968		
Smearing $\tau\tau \to \pi\pi$	Amplitude	u	0.0289675	0.00132437	
	Offset	w	0.0712988	0.000965612	
	CP-mixing angle	ϕ_τ	$-1.68492°$	$1.33126°$	$0°$
	Asymmetry	$A^{aa'}$	$25.8648\,\%$	$0.283953\,\%$	
	Goodness of the fit	$\chi^2/$d.o.f	1.44474		

B. Second appendix

No smearing $\tau\tau \to \pi\ell$	Amplitude	u	0.0182495	0.000469027	
	Offset	w	0.0713511	0.000334018	
	CP-mixing angle	ϕ_τ	$-89.241°$	$0.734932°$	$\pm 90°$
	Asymmetry	$A^{aa'}$	$16.2828\,\%$	$0.103148\,\%$	
	Goodness of the fit	$\chi^2/\text{d.o.f}$	1.64461		
Smearing $\tau\tau \to \pi\ell$	Amplitude	u	0.00966858	0.000570194	
	Offset	w	0.0713876	0.000404348	
	CP-mixing angle	ϕ_τ	$-91.5985°$	$1.69198°$	$\pm 90°$
	Asymmetry	$A^{aa'}$	$8.62224\,\%$	$0.126641\,\%$	
	Goodness of the fit	$\chi^2/\text{d.o.f}$	0.588643		

Table B.7.: Fit parameters.

Smear	Parameter	Name	Value	Error	Exp. Value
None	Amplitude	u	0.0499439	0.00104631	
	Offset	w	0.0714149	0.000802239	
	CP-mixing angle	ϕ_τ	$-0.335638°$	$0.603903°$	$0°$
	Asymmetry	$A^{aa'}$	$44.5219\,\%$	$0.20177\,\%$	$50\,\%$
	Goodness of the fit	$\chi^2/\text{d.o.f}$	1.4968		
$n_\pm$	Amplitude	u	0.0499347	0.00104673	
	Offset	w	0.0714244	0.000802295	
	CP-mixing angle	ϕ_τ	$-0.338535°$	$0.603928°$	$0°$
	Asymmetry	$A^{aa'}$	$44.5078\,\%$	$0.201867\,\%$	
	Goodness of the fit	$\chi^2/\text{d.o.f}$	1.39547		
$q_\pm, E_\pm$	Amplitude	u	0.0280554	0.00134566	
	Offset	w	0.0713929	0.000973198	
	CP-mixing angle	ϕ_τ	$1.92227°$	$1.3782°$	$0°$
	Asymmetry	$A^{aa'}$	$25.0173\,\%$	$0.289088\,\%$	
	Goodness of the fit	$\chi^2/\text{d.o.f}$	0.761615		
All	Amplitude	u	0.0289677	0.00132437	
	Offset	w	0.0712988	0.000965612	
	CP-mixing angle	ϕ_τ	$-1.68482°$	$1.33126°$	$0°$
	Asymmetry	$A^{aa'}$	$25.865\,\%$	$0.283953\,\%$	
	Goodness of the fit	$\chi^2/\text{d.o.f}$	1.44474		

Table B.8.: Fit parameters.

The Table (B.7) shows the fit parameters and CP mixing angles for the different decay modes (with or without smearing), calculated with the IP method. The corresponding plot is given by Figure (5.13). The Table (B.8) corresponds to Figure (5.14).

The names of the used samples are the following:

ggH	Had-Had
CP-even	mc15_13TeV.341124.PowhegPythia8EvtGen_CT10_AZNLOCTEQ6L1_ ggH125_tautauhh.merge.DAOD_HIGG4D3.e3935_s2608_s2183_r6765_ r6282_p2608
CP-odd	mc15_13TeV.341905.PowhegPythia8EvtGen_CT10_AZNLOCTEQ6L1_ ggH125_tautauhh_CPodd.merge.DAOD_HIGG4D3.e4103_s2608_r6765_ r6282_p2608
CP-unpol	mc15_13TeV.341907.PowhegPythia8EvtGen_CT10_AZNLOCTEQ6L1_ ggH125_tautauhh_unpol.merge.DAOD_HIGG4D3.e4103_s2608_r6765_ r6282_p2608
VBF	Had-Had
CP-even	mc15_13TeV.341157.PowhegPythia8EvtGen_CT10_AZNLOCTEQ6L1_ VBFH125_tautauhh.merge.DAOD_HIGG4D3.e3888_s2608_s2183_ r6765_r6282_p2608
CP-odd	mc15_13TeV.341911.PowhegPythia8EvtGen_CT10_AZNLOCTEQ6L1_ VBFH125_tautauhh_CPodd.merge.DAOD_HIGG4D3.e4103_s2608_ r6765_r6282_p2608
CP-unpol	mc15_13TeV.341913.PowhegPythia8EvtGen_CT10_AZNLOCTEQ6L1_ VBFH125_tautauhh_unpol.merge.DAOD_HIGG4D3.e4103_s2608_ r6765_r6282_p2608
$Z \to \tau\tau$	Had-Had
	mc15_13TeV.361108.PowhegPythia8EvtGen_AZNLOCTEQ6L1_ Ztautau.merge.DAOD_HIGG4D3.e3601_s2726_ r7326_r6282_p2608

ggH	Lep-Had
CP-even	mc15_13TeV.341123.PowhegPythia8EvtGen_CT10_AZNLOCTEQ6L1_ ggH125_tautaulh.merge.DAOD_HIGG4D2.e3935_s2608_s2183_ r6765_r6282_p2608
CP-odd	mc15_13TeV.341902.PowhegPythia8EvtGen_CT10_AZNLOCTEQ6L1_ ggH125_tautaulh_CPodd.merge.DAOD_HIGG4D2.e4103_s2608_ r6765_r6282_p2608
CP-unpol	mc15_13TeV.341904.PowhegPythia8EvtGen_CT10_AZNLOCTEQ6L1_ ggH125_tautaulh_unpol.merge.DAOD_HIGG4D2.e4103_s2608_ r6765_r6282_p2608
VBF	Lep-Had
CP-even	mc15_13TeV.341156.PowhegPythia8EvtGen_CT10_AZNLOCTEQ6L1_ VBFH125_tautaulh.merge.DAOD_HIGG4D2.e3888_s2608_s2183_ r6765_r6282_p2608
CP-odd	mc15_13TeV.341908.PowhegPythia8EvtGen_CT10_AZNLOCTEQ6L1_ VBFH125_tautaulh_CPodd.merge.DAOD_HIGG4D2.e4103_s2608_ r6765_r6282_p2608
CP-unpol	mc15_13TeV.341910.PowhegPythia8EvtGen_CT10_AZNLOCTEQ6L1_ VBFH125_tautaulh_unpol.merge.DAOD_HIGG4D2.e4103_s2608_ r6765_r6282_p2608
$Z \to \tau\tau$	Lep-Had
	mc15_13TeV.361108.PowhegPythia8EvtGen_AZNLOCTEQ6L1_ Ztautau.merge.DAOD_HIGG4D2.e3601_s2726_ r7326_r6282_p2608

Bibliography

[1] S. Berge, W. Bernreuther, S. Kirchner, *Prospects of constraining the Higgs boson's C P nature in the tau decay channel at the LHC*, Phys. Rev. D **92(9)**, 096012 (2015)

[2] S. L. Glashow, *Partial-symmetries of weak interactions*, Nucl. Phys. **22**, 579 (1961)

[3] S. Weinberg, *A Model of Leptons*, Phys. Rev. Lett. **19**, 1264 (1967)

[4] A. Salam, *Weak and Electromagnetic Interactions*, in N. Svartholm, editor, *Elementary particle theory*, pages 367–377, Almquist & Wiksell (1968)

[5] H. Fritzsch, M. Gell-Mann, H. Leutwyler, *Advantages of the color octet gluon picture*, Phys. Lett. B **47(4)**, 365 (1973)

[6] ATLAS Collaboration, *Observation of a new particle in the search for the Standard Model Higgs boson with the ATLAS detector at the LHC*, Phys. Lett. B **716(1)**, 1 (2012)

[7] CMS Collaboration, *Observation of a new boson at a mass of 125 GeV with the CMS experiment at the LHC*, Phys. Lett. B **716(1)**, 30 (2012)

[8] DØ Collaboration, S. Abachi, et al., *Observation of the Top Quark*, Physical Review Letters **74**, 2632 (1995)

[9] CDF Collaboration, F. Abe, et al., *Observation of top quark production in $\bar{p}p$ collisions*, Phys. Rev. Lett. **74**, 2626 (1995)

[10] DONUT Collaboration, K. Kodama, et al., *Observation of tau neutrino interactions*, Phys. Lett. B **504**, 218 (2001)

[11] R. S. Huerfano, M. Khovanov, *A Category for the Adjoint Representation*, J. Alg. **246(2)**, 514 (2001)

[12] F. Englert, R. Brout, *Broken Symmetry and the Mass of Gauge Vector Mesons*, Phys. Rev. Lett. **13**, 321 (1964)

Bibliography

[13] P. W. Higgs, *Broken Symmetries and the Masses of Gauge Bosons*, Phys. Rev. Lett. **13**, 508 (1964)

[14] K. A. Olive, et al. (Particle Data Group), *Review of Particle Physics, STATUS OF HIGGS BOSON PHYSICS*, Chin. Phys. C **38**, 090001 (2013)

[15] S. Hannestad, *Dark energy and dark matter from cosmological observations*, Int. J. Mod. Phys. A **21**, 1938 (2006)

[16] S. D. Bass, *Vacuum energy and the cosmological constant*, Mod. Phys. Lett. A **30**, 1540033-321 (2015)

[17] Y. Fukuda, et al., *Evidence for Oscillation of Atmospheric Neutrinos*, Phys. Rev. Lett. **81**, 1562 (1998)

[18] M. H. Ahn, et al., *Indications of Neutrino Oscillation in a 250 km Long-Baseline Experiment*, Phys. Rev. Lett. **90**, 041801 (2003)

[19] R. D. Peccei, *The Strong CP Problem and Axions*, in M. Kuster, G. Raffelt, B. Beltrán, editors, *Axions*, volume 741 of *Lecture Notes in Physics, Berlin Springer Verlag*, page 3 (2008)

[20] J. Bordes, H.-M. Chan, S. T. Tsou, *a Solution to the Strong CP Problem Transforming the Theta Angle to the KM Cp-Violating Phase*, Int. J. Mod. Phys. A **25**, 5897 (2010)

[21] J. R. Ellis, *Limits of the standard model*, in *PSI Zuoz Summer School on Exploring the Limits of the Standard Model Zuoz, Engadin, Switzerland, August 18-24, 2002* (2002)

[22] ATLAS Collaboration, *Search for TeV-scale gravity signatures in high-mass final states with leptons and jets with the ATLAS detector at $\sqrt{s} = 13$ TeV*, Phys. Lett. B **760**, 520 (2016)

[23] S. Di Chiara, L. Marzola, M. Raidal, *First interpretation of the 750 GeV diphoton resonance at the LHC*, Phys. Rev. D **93(9)**, 095018 (2016)

[24] L. Rossi, E. Todesco, *Conceptual design of 20 T dipoles for high-energy LHC*, in *Proceedings, EuCARD-AccNet-EuroLumi Workshop: The High-Energy Large Hadron Collider (HE-LHC10): Villa Bighi, Malta, Republic of Malta, October 14-16, 2010* (2011)

[25] A. Djouadi, G. Moreau, *The couplings of the Higgs boson and its CP properties from fits of the signal strengths and their ratios at the 7+8 TeV LHC*, Eur. Phys. J. C **73**, 2512 (2013)

[26] ATLAS Collaboration, *Evidence for the spin-0 nature of the Higgs boson using ATLAS data*, Phys. Lett. B **726**, 120 (2013)

[27] J. Ellis, T. You, *Updated global analysis of Higgs couplings*, JHEP **6**, 103 (2013)

[28] J. Baglio, et al., *The measurement of the Higgs self-coupling at the LHC: theoretical status*, JHEP **4**, 151 (2013)

[29] S. Berge, W. Bernreuther, J. Ziethe, *Determining the CP Parity of Higgs Bosons via Their τ Decay Channels at the Large Hadron Collider*, Phys. Rev. Lett. **100(17)**, 171605 (2008)

[30] S. Berge, W. Bernreuther, S. Kirchner, *Determination of the Higgs CP-mixing angle in the tau decay channels at the LHC including the Drell-Yan background*, Eur. Phys. J. C **74**, 3164 (2014)

[31] S. Berge, et al., *How to pin down the CP quantum numbers of a Higgs boson in its τ decays at the LHC*, Phys. Rev. D **84(11)**, 116003 (2011)

[32] S. Berge, W. Bernreuther, *Determining the CP parity of Higgs bosons at the LHC in the τ to 1-prong decay channels*, Phys. Lett. B **671**, 470 (2009)

[33] G. R. Bower, et al., *Measuring the Higgs boson's parity using $\tau \to \rho\nu$*, Phys. Lett. B **543**, 227 (2002)

Acknowledgements

I would like to thank Prof. Dr. Arnulf Quadt for being the first referee of this thesis. He gave me the opportunity to write my bachelor thesis in particle physics. I would like to thank Prof. Dr. Stan Lai for being the second referee. Thanks also go out to Dr. Zinonas Zinonos for being my supervisor.

I would like to expressly thank Antonio De Maria for all the helpful discussions and for proof-reading this thesis.

Erklärung nach §13(9) der Prüfungsordnung für den Bachelor-Studiengang Physik und den Master-Studiengang Physik an der Universität Göttingen:

Hiermit erkläre ich, dass ich diese Abschlussarbeit selbständig verfasst habe, keine anderen als die angegebenen Quellen und Hilfsmittel benutzt habe und alle Stellen, die wörtlich oder sinngemäß aus veröffentlichten Schriften entnommen wurden, als solche kenntlich gemacht habe.

Darüberhinaus erkläre ich, dass diese Abschlussarbeit nicht, auch nicht auszugsweise, im Rahmen einer nichtbestandenen Prüfung an dieser oder einer anderen Hochschule eingereicht wurde.

Göttingen, den 28. Oktober 2016

(Paul Konstantin Krug)